Simulating Thermal Radiation Transport in Molten Salt Reactors

AP3902: Master Thesis Project

R. B. Bissumbhar

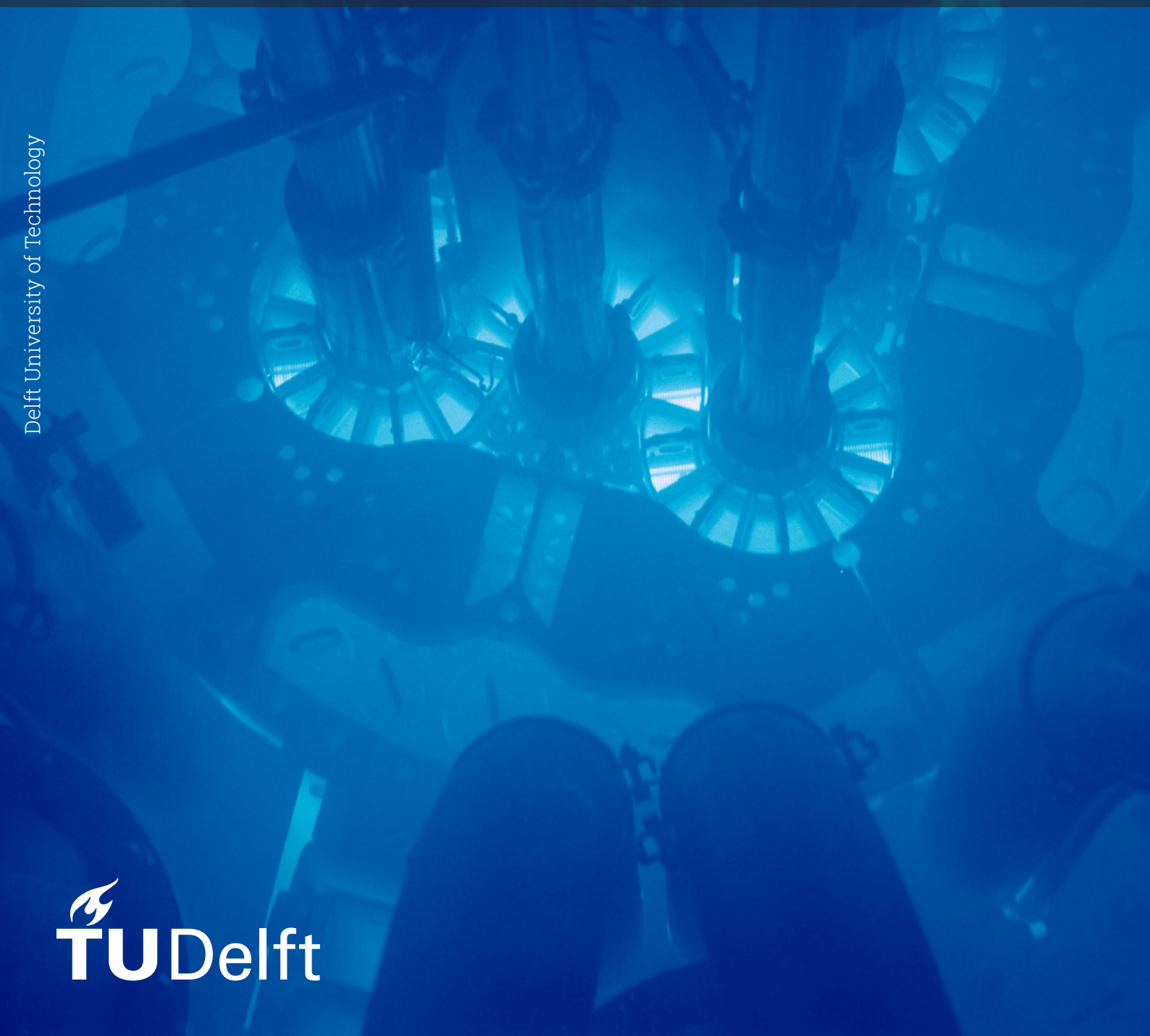

Delft University of Technology

TU Delft

Simulating Thermal Radiation Transport in Molten Salt Reactors

by

R. B. Bissumbhar

to obtain the degree of Master of Science
at the Delft University of Technology,
to be defended publicly in September, 2023

Student number:	4565606	
Project duration:	December 19, 2022 – September 8, 2023	
Thesis committee:	Dr. ir. D. Lathouwers,	TU Delft, supervisor
	T.B.D.,	TU Delft
	T.B.D.,	TU Delft

Cover: Advanced Test Reactor core, Idaho National Laboratory by Argonne National Laboratory (Modified)

TU Delft

Summary

Molten Salt Reactors (MSRs) can reduce the creation of nuclear waste and safety concerns involved with the current reactors while keeping the benefits of nuclear energy. MSRs operate at higher temperatures compared to the current water-based reactors. At higher temperatures, thermal radiation starts to play a role, and molten salts, like FLiNaK used in this study, are semi-transparent to thermal radiation, unlike water.

To determine the effect of thermal radiation, a simulation model was created to simulate the Flat Channel geometry used in the SWATH facility, which researches thermal radiation in MSRs. The model determines the thermal radiation inside the Flat Channel and determines the temperature distribution using conduction and convection alongside thermal radiation. The FLiNaK can absorb and emit thermal radiation, like the boundary walls of the Flat Channel that also diffusely and specularly reflect incoming thermal radiation.

The temperature difference on the upper wall of the Flat Channel, caused by thermal radiation coming from the heated lower wall of the channel, was looked at. A maximum increase of 3% in the temperature caused by thermal was seen in some areas of the upper wall. Higher FLiNaK temperatures flowing into the Flat Channel and higher bottom wall temperatures increase the effect of thermal radiation transport. The lower the inlet velocity, the higher the effect of thermal radiation transport is up to a certain point, after which the influence of thermal radiation decreases.

Contents

Nomenclature

Abbreviations

Abbreviation	Definition
FLiBe	LiF-BeF_2
FLiNaK	LiF-NaF-KF
MSR	Molten Salt Reactor
PWR	Pressurised Water Reactor
RTE	Radiative Transfer Equation or Radiation Transport Equation
SWATH	Salt at Wall: Thermal Exchanges

Symbols

Symbol	Definition	Unit
B_E	Spectral Black-body Radiative Intensity	[W·sr^{-1}·m^{-2}·J^{-1}]
B_λ	Spectral Black-body Radiative Intensity	[W·sr^{-1}·m^{-2}·m^{-1}]
B_ν	Spectral Black-body Radiative Intensity	[W·sr^{-1}·m^{-2}·Hz^{-1}]
c	Speed of Light	[m·s^{-1}]
c_0	Speed of Light in a Vacuum	[m·s^{-1}]
c_v	Specific Heat Capacity at constant Volume	[J·kg^{-1}·K^{-1}]
c_p	Specific Heat Capacity at constant Pressure	[J·kg^{-1}·K^{-1}]
E	Photon Energy	[J] or [eV]
h	Planck's Constant	[J·Hz^{-1}]
h	Height	[m]
I	Radiative Intensity	[W·sr^{-1}·m^{-2}]
I_b	Black-body Radiative Intensity	[W·sr^{-1}·m^{-2}]
I_{bE}	Spectral Black-body Radiative Intensity	[W·sr^{-1}·m^{-2}·J^{-1}]
I_E	Spectral Radiative Intensity	[W·sr^{-1}·m^{-2}·J^{-1}]
I_ν	Spectral Radiative Intensity	[W·sr^{-1}·m^{-2}·Hz^{-1}]
k_B	Boltzmann Constant	[J·K^{-1}]
$\dot{m}$	Mass Flow Rate	[kg·s^{-1}]
n	Refractive Index	[-]
n	Number of Directions	[-]
$\hat{\boldsymbol{n}}$	Surface Unit Vector	[-]
N	Discrete Ordinates Method Order	[-]
p	Pressure	[Pa]
$\boldsymbol{q}_R$	Total Heat Flux Vector	[W·m^{-2}]
$\boldsymbol{q}_R$	Conductive Heat Flux Vector	[W·m^{-2}]
$\boldsymbol{q}_R$	Radiative Heat Flux Vector	[W·m^{-2}]
$\dot{Q}'''$	Heat Generation Rate	[W·m^{-3}
$\boldsymbol{r}$	Position Vector	[m]

Symbol	Definition	Unit
$\boldsymbol{r}_w$	Position Vector at the Wall	[m]
t	Time	[s]
S_N	Discrete Ordinates Method	[-]
T	Temperature	[K]
u	Internal Energy	[J·kg^{-1}]
U_A	Inlet Velocity	[m·s^{-1}]
v	Velocity Field	[m·s^{-1}]
v_p	Poiseuille Velocity profile	[m·s^{-1}]
v_x	Velocity Component in the x-direction	[m·s^{-1}]
$\dot{V}$	Flow Rate	[m^3·s^{-1}]
w_i	Quadrature Weights	[-]
$\boldsymbol{\delta}$	Unit Tensor	[-]
ε	Emittance or Emissivity	[-]
η	Direction cosine in the y-direction	[-]
λ	Wavelength	[m]
λ	Thermal COnductivity	[W m^{-1} K^{-1}]
μ	Direction cosine in the z-direction	[-]
μ	Dynamic Viscosity	[Pa·s]
ν	Frequency	[Hz]
ξ	Direction cosine in the x-direction	[-]
ρ	Density	[kg·m^{-3}]
ρ^d	Diffuse Reflectance or Reflectivity	[-]
ρ^s	Specular Reflectance or Reflectivity	[-]
σ_a	Linear Absorption coefficient	[m^{-1}]
σ_{aE}	Spectral Linear Absorption coefficient	[m^{-1}·J^{-1}]
σ_s	Isotropic Scatter coefficient	[m^{-1}]
σ_{sE}	Spectral Isotropic Scatter coefficient	[m^{-1}·J^{-1}]
σ_t	Total Attenuation coefficient	[m^{-1}]
σ_{tE}	Spectral Total Attenuation coefficient	[m^{-1}·J^{-1}]
Φ	Viscous Dissipation function	[W·s·kg^{-1}·m^{-2}]
$\hat{\boldsymbol{\Omega}}$	Direction Unit Vector	[-]

1 Introduction

1.1. Nuclear Energy

The world is facing one of its biggest challenges, namely global warming. This issue is why energy sources that do not rely on fossil fuels are becoming increasingly important. One of these alternative sources is nuclear energy. Another benefit of nuclear power is energy independence by reducing the reliance on fossil fuels from foreign countries.

Nuclear energy is a clean source of energy that emits no air pollutants and is a reliable source of energy that does not depend on environmental factors such as wind speed and solar intensity, like wind energy and solar energy [1]. Nuclear power is usable in the electrical grid to help deal with the intermittency of aforementioned renewable energy sources but is currently predominantly used as a baseload.

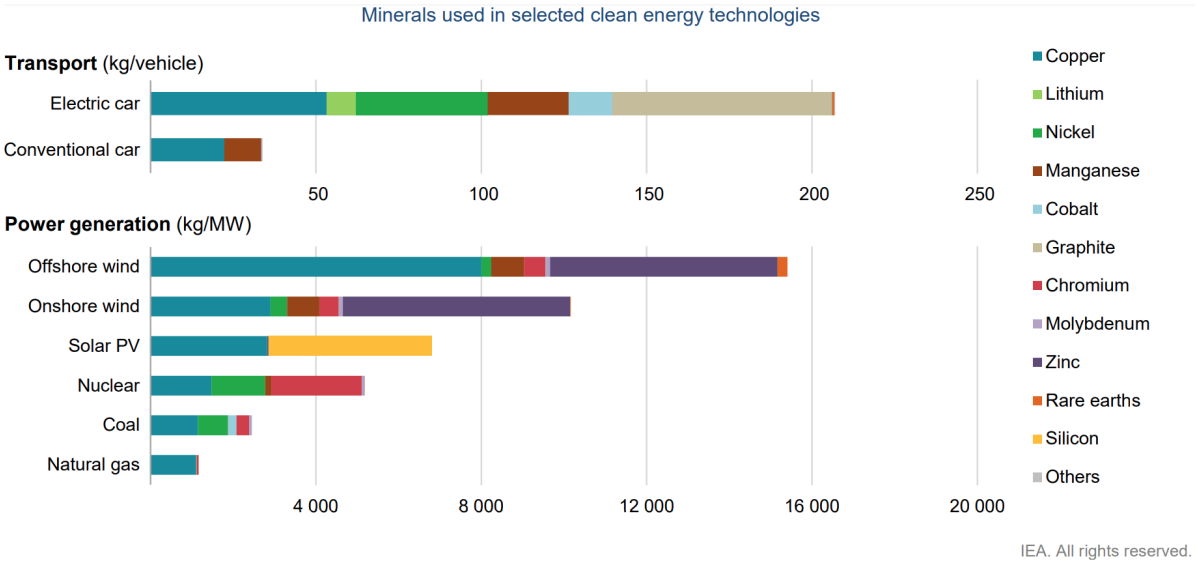

Figure 1.1: This figure shows the amount of minerals used in kilograms to produce a vehicle or to build one megawatt of power generation. Nuclear power generation uses from left to right: copper, nickel, manganese, chromium, molybdenum, and a tiny sliver of rare earth metals [2].

The amount of minerals (excluding steel and aluminium) used to produce energy is advantageous in nuclear power generation compared to photovoltaic solar panels and wind turbines.

Figure 1.1 shows the amount of minerals (in kilograms) used to generate one megawatt of power. We see that wind and solar power use more minerals than nuclear power to generate the same amount of power. The type of minerals (apart from the small number of rare earth metals) used for nuclear power are non-critical, so they are not at risk of depleting the supply of these scarce resources, like solar and wind power do [3].

Producing nuclear energy requires nuclear (fission) reactors. These reactors also have downsides, like the production of nuclear waste and devastatingly consequential safety concerns. The results of negligence toward safety can result in events like Chornobyl and Fukushima. For these and other reasons, it is desirable to improve the design of nuclear reactors by making them more efficient and tackling the issues mentioned. One of these improved designs is the Molten Salt Reactor (MSR).

1.2. Molten Salt Reactors (MSRs)

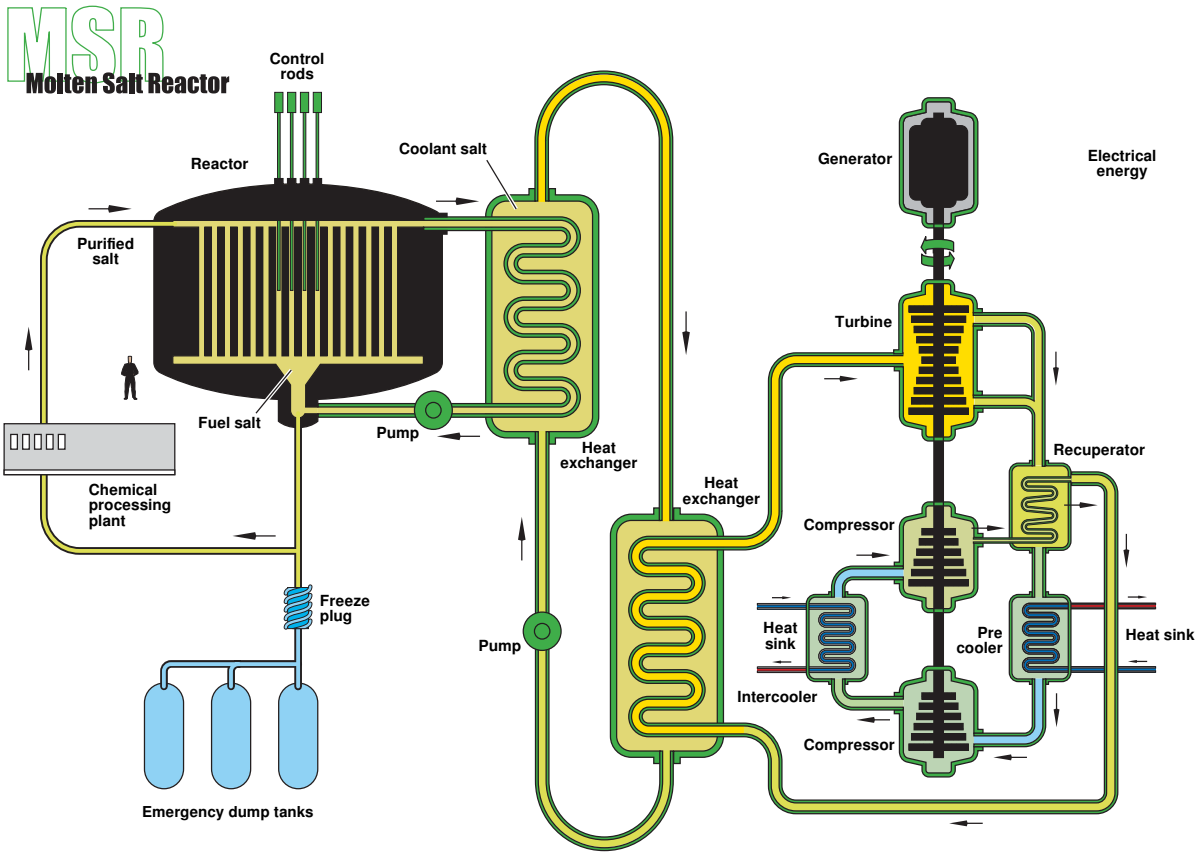

Figure 1.2: A schematic drawing of a Molten Salt Reactor used to generate electricity [4].

Molten Salt Reactors are generation IV nuclear fission reactors that use molten salt. The molten salt acts as the coolant and fuel, distinct from most regular reactors where water is the coolant and the (solid) fuel is inside the fuel rods. Different types of fluoride or chloride salts can be used in MSRs. Some of the specific salts used can be found in Section 2.4. Just like regular electric power-generating reactors, MSRs can use steam turbines to generate electricity. The molten salt can be used to heat water (in a secondary circuit) using a heat exchanger and turn the water into steam which is fed to a steam turbine.

The fuel is dissolved inside the molten salt and can fission inside the reactor seen in the schematic shown in Figure 1.2. The fission reaction leaves, among others, non-usable waste products that can be taken out using a chemical processing plant where new fuel can be added as well. This process is called online refuelling/recycling, which allows the reactor to operate longer than conventional reactors that have to shut down to refuel. The fuel used in MSRs doesn't need to be U-235, as the MSR can function as a breeder reactor, thus allowing it to use the more available thorium or radioactive waste products as fuel [4].

The MSR operates at high temperatures of 500-700 degrees Celsius, but the salt can go up to 1400 degrees Celsius using atmospheric pressure [5][6]. This high operating temperature gives the benefit of greater efficiency in generating electricity. They also have low operating pressures (ambient pressure), which decrease the risk of equipment malfunction, and the risk of an explosion, as might happen in Pressurised Water Reactors (PWRs) that operate at 150 times the atmospheric pressure [4][5].

When the molten salt heats up, the fuel mixture becomes less reactive due to a negative temperature coefficient of reactivity [5]. The negative coefficient is better for the safety of the MSR. Another safety feature in the design of the MSR is the freeze plug, seen in Figure 1.2. When a critical temperature is achieved, the freeze plug melts and drains the salt into emergency dump tanks using only gravity. The emergency tanks are designed in such a way that a chain reaction is not possible [4].

The MSR also has drawbacks. Molten salts can be corrosive and will therefore degrade materials. Also, since the MSR can be used as a breeder reactor, it can create isotopes usable for nuclear proliferation [4]. Further, online refuelling requires a chemical plant that can handle radioactive products, which yields a safety risk and expenditure [4]. Due to the high temperatures and the use of semi-transparent liquid salt, the mechanism of heat transport via thermal radiation might play an important role. The heat flux caused by thermal radiation scales with temperature to the fourth power, as opposed to the linearly scaling conduction and convection.

Thermal radiation (in reactors) falls in the infrared spectrum. Water is an excellent absorber of infrared radiation. Even merely water mist is a highly effective fire-protection agent [7]. The absorption coefficient of liquid water in Figure 1.3 shows the high absorption values in the infrared regions. It can be concluded that water is opaque to thermal radiation, which might not be the case for semi-transparent molten salt. This semi-transparency is a crucial point of differentiation of MSRs with water reactors. Due to the high absorption of thermal radiation by water, thermal radiation can only travel a minuscule distance which causes local heat changes and heat transport by thermal radiation to become unimportant. Thermal radiation travelling further away can be possible for MSRs, where thermal radiation transport can become an essential mechanism. Thus the need for understanding this mechanism also becomes important. The SAMOSAFER project studies the effect of thermal radiation transport and other safety concerns in MSRs.

1.3. SAMOSAFER

SAMOSAFER is a project that aims to develop and demonstrate new safety barriers for more controlled behaviour of Molten Salt Reactors in severe accidents, based on new simulation models and tools validated with experiments. The grand objective is to ensure that the MSR can comply with all expected regulations in 30 years [9]. This project is an international cooperation lead by TU Delft.

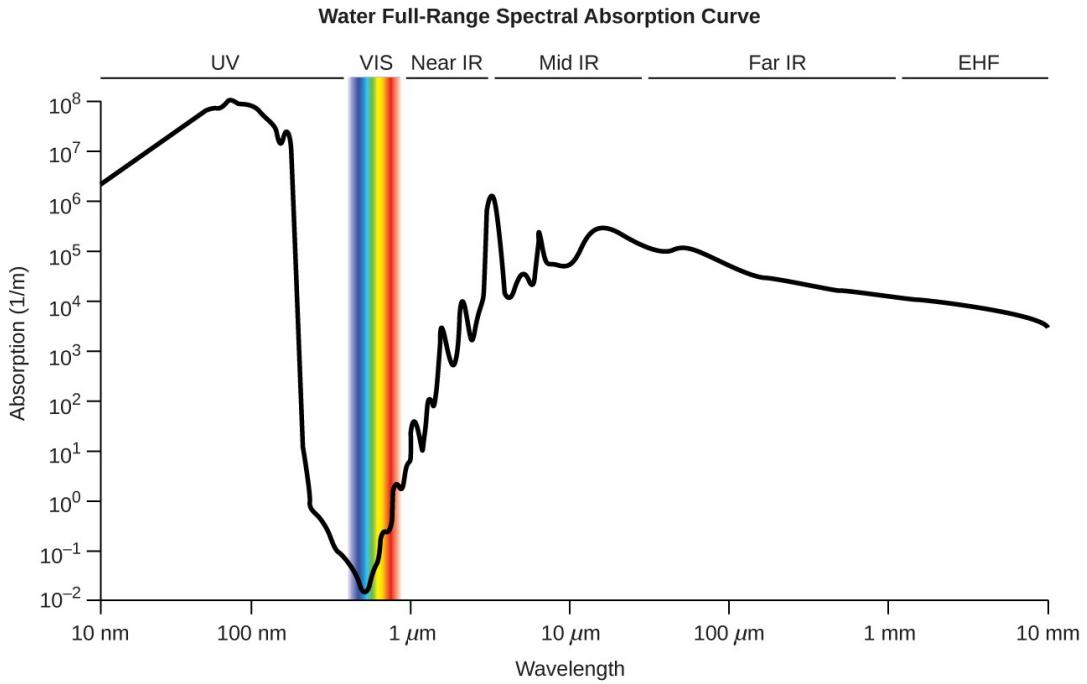

Figure 1.3: The plot shows the extent of light absorption versus wavelength for water. Absorption is reported in reciprocal meters and corresponds to the inverse of the distance light may travel through water before its intensity is diminished by 1/e (37%) [8].

1.3.1. SWATH

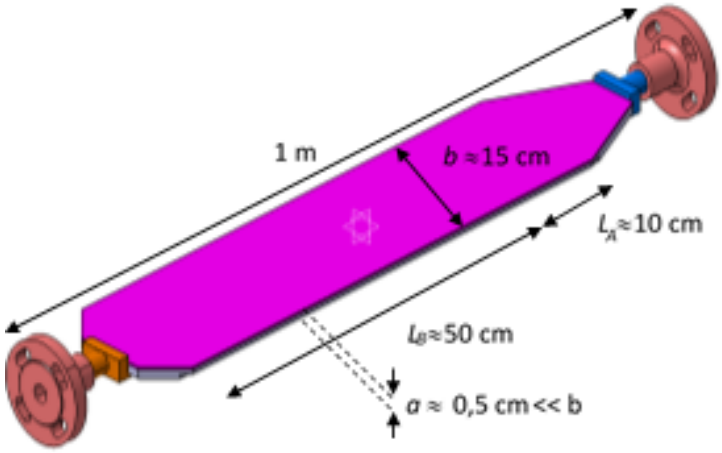

Figure 1.4: Approximate sketch of the Flat Channel geometry [10].

The ”Salt at Wall: Thermal ExcHanges” (SWATH) facility aims to study some of the specific molten salt phenomena and flow conditions that could exist during certain accidental conditions. The relevant test setup to this thesis in SWATH is the flat channel geometry. In this geometry, molten FLiNaK salt flows through a closed flat channel formed by two large plates at different temperatures. It operates between temperatures of about 500 and 600 °C with possible volumetric flow rates between 0.5 and 8 L/min.

The Flat Channel geometry is used to investigate the effect of radiative heat transfer by looking if thermal radiation can have a noticeable effect on the upper wall when the bottom wall is

heated. Figure 1.4 shows an approximate sketch of this setup. Flow diffusers are put at both of the tapered ends of the channel to help the development of the flow develop faster. For the simulation in this thesis, a simplified geometry of the flat channel was used, which can be seen in Figure 5.2.

1.4. Goal

The purpose of the thesis is to create a simulation model to gain a better understanding of thermal radiation in Molten Salt Reactors. To achieve the goal of this thesis, various sub-goals have been created, which are listed below.

- Learn about the physics of thermal radiation transport:
    - What is and causes thermal radiation?
    - How does radiation behave in substances?
    - Is it different from other types of transport?

- Determine the role of thermal radiation in molten salt:
    - What mechanism differ between molten salt and water?
    - What affects thermal radiation transport in molten salt?
    - Is its role negligible?

- Learn and implement about simulation methods regarding thermal radiation:
    - What numerical methods exist to simulate thermal radiation?
    - How to determine if the simulation is correct?

2

Thermal Radiation Transport

Heat transfer happens through the following three mechanisms: conduction (diffusion), convection, and radiation. In this chapter, we'll focus on heat transfer via thermal radiation.

Thermal radiation is electromagnetic radiation (or photons) emitted by all matter with a non-zero temperature, from ants to whales and grains of sand to (theoretically) even black holes. The source of the emitted radiation is a combination of electronic and molecular oscillations and transitions in the emitting material, as well as lattice vibrations [11]. The emitted photon's energy depends on its frequency ν via the relationship $E = h\nu$, where h is Planck's constant. This photon can travel through space with the speed of light without needing a medium, unlike convection and conduction, which require a medium. While a photon doesn't require a medium to travel, it can be affected by the properties of the medium it's travelling through. It can be reflected or attenuated by the medium. If all photons pass through a medium without attenuation, it's called *transparent*. A medium that absorbs all the photons travelling through it is called *opaque*. And lastly, a partially attenuating medium is called *semi-transparent* [12].

To determine how much thermal radiation an object gives off, we first need to know what type of object we are looking at. We can place objects or bodies in three denominations: black, grey, and white. A perfect black body absorbs all incident radiation, a grey body absorbs and reflects incident radiation, and an ideal white body only reflects all incident radiation. The emissivity ε of that object characterises the blackness of that body. A black body has an emissivity equal to one, a grey body can have an emissivity between zero and one, and a white body has an emissivity (or emittance) equal to zero. The thermal radiation per photon frequency, in W·sr^{-1}·m^{-2}·Hz^{-1}, emitted by an object is related to $\varepsilon B_\nu(\nu, T)$, where $B_\nu(\nu, T)$ is the spectral radiative intensity given off by a black body in units of W·sr^{-1}·m^{-2}·Hz^{-1}, and T is the temperature in Kelvin. The following section discusses black-body radiation.

2.1. Black-body Radiation

Black-body radiation, as the name implies, is thermal radiation given off by black bodies. The amount of black-body radiation emitted is described by Planck's law. Equation 2.1 shows this law. Planck's law gives the spectral radiative intensity of a black body $B_\nu(\nu, T)$. Radiative intensity is the amount of radiative energy flow per time per area normal to the rays per solid angle (per frequency or another unit if it's the spectral intensity)

$$B_\nu(\nu, T) = \frac{2hn^2}{c_0^2} \frac{\nu^3}{e^{h\nu/k_B T} - 1}, \tag{2.1}$$

where n is the refractive index, c_0 is the speed of light in a vacuum, and k_B is the Boltzmann constant. While we could use equation 2.1, it is preferred to describe the spectral radiative intensity as a function of the energy E, instead of frequency ν. Equation 2.2 shows Planck's law with the spectral radiative intensity of a black body $B_E(E,T)$. The energy E is the energy of the photon emitted by the black body in Joules.

$$B_E(E,T) = \frac{2n^2}{h^3 c_0^2} \frac{E^3}{e^{E/k_B T} - 1} \tag{2.2}$$

Figure 2.1 shows equation 2.2 using temperatures near the operating temperatures of the SWATH experiment mentioned in Section 5.1, which are between 500 and 650 degrees Celsius [10].

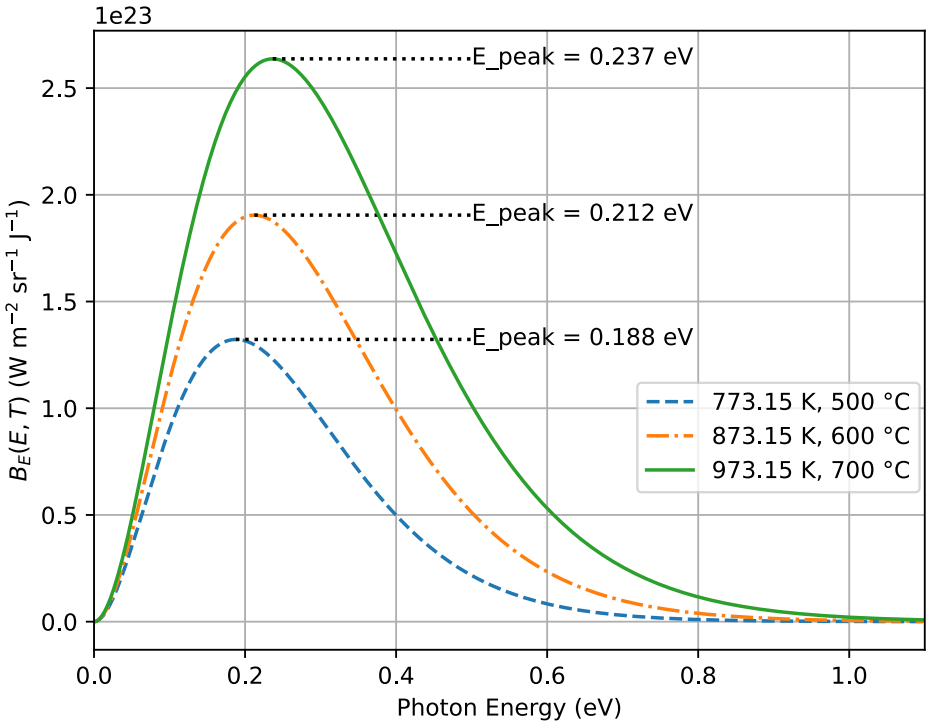

Figure 2.1: Planck's law for black bodies is shown using temperatures of 500, 600, and 650 degrees Celsius. The photon energy in electron volts is on the horizontal axis, and the corresponding spectral radiative intensity $B_E(E,T)$ is on the vertical axis. The photon energy at the maximum spectral irradiance is also visible. Plank's law with $B_\lambda(\lambda,T)$ can be found in Figure A.1.

2.2. Radiation Transport Equation (RTE)

Now that the source of thermal radiation has been explained, the transport of this radiation also needs to be discussed. This transfer can be described through the Radiation Transport Equation (RTE) in participating media, meaning the medium interacts with the thermal radiation by absorption, emission, and scatter. Equation 2.11 at the end of this section shows the complete RTE, but first, further explanation of the radiative intensity $I(\boldsymbol{r}, \hat{\boldsymbol{\Omega}}, t)$ is needed.

As mentioned in Section 5.2, radiative intensity $I(\boldsymbol{r}, \hat{\boldsymbol{\Omega}}, t)$ is the amount of radiative energy flow per time per area normal to the rays per solid angle. $I(\boldsymbol{r}, \hat{\boldsymbol{\Omega}}, t)$ is a function of position $\boldsymbol{r}$,

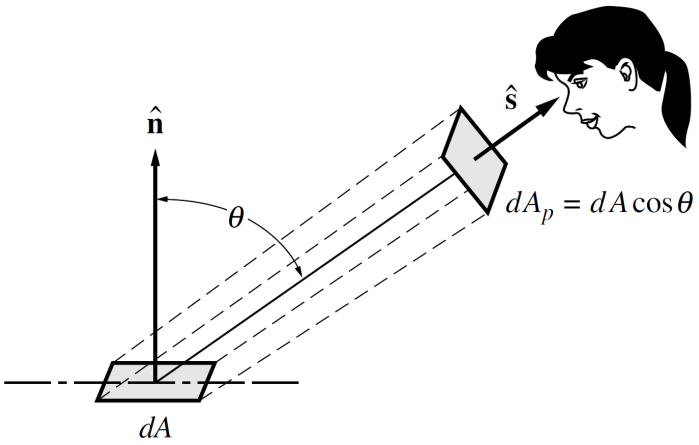

Figure 2.2: Relationship between black-body emissive power and radiative intensity. dA is the area that emits black-body radiation and dA_p is the projected area of dA normal to the rays in direction $\hat{s}$. Here $\hat{n}$ is the normal vector of dA and θ the angle between $\hat{n}$ and $\hat{s}$. [12]

direction (or solid angle) $\hat{\mathbf{\Omega}}$, and time t. Radiative intensity is not the same as the total heat flux emitted by a surface, what you might logically expect, which is called the total emissive power. More clearly, total emissive power is the radiated energy per time per surface area. The difference is the distinction between surface area and area normal to the rays. Figure 2.2 shows the relationship between the emitting area and the area normal to the rays. Radiative intensity is used instead of emissive power because emissive power is inadequate in describing the directional dependence of radiation [12].

There exist mechanisms that reduce and augment thermal radiation. Of the earlier three possible interactions in participating media, absorption and scattering can attenuate thermal radiation. The change in radiation caused by absorption over a path length dr is

$$(dI_E)_{\text{abs}} = -\sigma_{aE} I_E dr, \tag{2.3}$$

where σ_{aE} is the (linear) absorption coefficient, which depends on the photon energy, and I_E is the (linear) absorption coefficient, which depends on the photon energy, and I_E is the spectral radiative intensity. We get the total radiative intensity by integrating over all possible energies: $I = \int I_E \, dE$. The attenuation by scattering is also called ”out-scattering” since the incoming radiation $I_E(\boldsymbol{r}, \hat{\mathbf{\Omega}}, t)$ deflects to a (different) direction $\hat{\mathbf{\Omega}}'$ which will decrease the intensity in $\hat{\mathbf{\Omega}}$. The change in radiation caused by out-scattering over a path length dr is

$$(dI_E)_{\text{out}} = -\sigma_{sE} I_E dr, \tag{2.4}$$

where σ_{aE} is the (linear) scattering coefficient, which also depends on the photon energy as denoted by the subscript E. The negative signs in equations 2.3 and 2.4 are due to their attenuating effects on the intensity. We can combine these two effects using $\sigma_{tE} = \sigma_{aE} + \sigma_{sE}$, which gives us the following change in the radiative intensity

$$(dI_E)_{\text{att}} = -\sigma_{tE} I_E dr. \tag{2.5}$$

Apart from attenuation, there is also augmentation in the form of emission and ”in-scatter”. Emission causes the following increase equally in every direction

$$(dI_E)_{\text{emi}} = \sigma_{aE} I_{bE} dr. \tag{2.6}$$

The other source of augmentation is in-scatter. Equation 2.7 shows the change in the intensity caused by in-scatter. We calculate in-scatter by integrating the intensities over all incoming directions $\hat{\mathbf{\Omega}}'$ using a weight function called the scattering phase function $\Phi_E(\hat{\mathbf{\Omega}}', \hat{\mathbf{\Omega}})$, which describes a ray from $\hat{\mathbf{\Omega}}'$ scattering into $\hat{\mathbf{\Omega}}$. We have isotropic scattering, so $\Phi_E(\hat{\mathbf{\Omega}}', \hat{\mathbf{\Omega}}) = 1$.

$$(dI_E)_{\text{ins}} = dr\frac{\sigma_{sE}}{4\pi}\int_{4\pi} I_E(\boldsymbol{r}, \hat{\mathbf{\Omega}}', t)\Phi_E(\hat{\mathbf{\Omega}}', \hat{\mathbf{\Omega}})\, d\Omega' \tag{2.7}$$

Now that the sources of attenuation and augmentation of thermal radiation have been considered, the RTE can be put together. We know that the change in intensity

$$dI_E = (dI_E)_{\text{att}} + (dI_E)_{\text{emi}} + (dI_E)_{\text{ins}}, \tag{2.8}$$

which can be rewritten as $dI_E = I_E(r+dr, \hat{\mathbf{\Omega}}, t+dt) - I_E(r, \hat{\mathbf{\Omega}}, t)$. Also, the $I_E(r+dr, \hat{\mathbf{\Omega}}, t+dt)$ part can be further expanded to

$$I_E(r+dr, \hat{\mathbf{\Omega}}, t+dt) = I_E(r, \hat{\mathbf{\Omega}}, t) + dt\frac{\partial I_E}{\partial t} + dr\frac{\partial I_E}{\partial r}. \tag{2.9}$$

Since thermal radiation is electromagnetic radiation which travels at the speed of light, it gives us the relation $dr = c\, dt$. If this relation is combined with equations 2.8 and 2.9, divided by dr, and $\partial I_E/\partial r$ is rewritten as $\hat{\mathbf{\Omega}} \cdot \nabla I_E(\boldsymbol{r}, \hat{\mathbf{\Omega}})$, it results in the final expression for the transient RTE

$$\frac{1}{c}\frac{\partial I_E(\boldsymbol{r}, \hat{\mathbf{\Omega}}, t)}{\partial t} + \frac{\partial I_E(\boldsymbol{r}, \hat{\mathbf{\Omega}}, t)}{\partial r} + \sigma_{tE} I_E(\boldsymbol{r}, \hat{\mathbf{\Omega}}, t) = \sigma_{aE} I_{bE}(\boldsymbol{r}, t) + \frac{\sigma_{sE}}{4\pi}\int_{4\pi} I_E(\boldsymbol{r}, \hat{\mathbf{\Omega}}', t)\, d\Omega'. \tag{2.10}$$

A quasi-steady form of the RTE also exists, where the time derivative and time dependence in the RTE disappear. dI_E/dr can similarly be rewritten as $\hat{\mathbf{\Omega}} \cdot \nabla I_E(\boldsymbol{r}, \hat{\mathbf{\Omega}})$, which gives

$$\hat{\mathbf{\Omega}} \cdot \nabla I_E(\boldsymbol{r}, \hat{\mathbf{\Omega}}) + \sigma_{tE} I_E(\boldsymbol{r}, \hat{\mathbf{\Omega}}) = \sigma_{aE} I_{bE}(\boldsymbol{r}) + \frac{\sigma_{sE}}{4\pi}\int_{4\pi} I_E(\boldsymbol{r}, \hat{\mathbf{\Omega}}')\, d\Omega', \tag{2.11}$$

showing the RTE in its quasi-steady form. The quasi-steady form of the RTE is valid for most engineering cases since the speed of light is so large compared to local time and length scales, allowing the time dependence to be neglected [12].

2.3. Boundary Conditions of the RTE

The quasi-steady form of the RTE (eq. 2.11) is a first-order integro-differential equation. We need to know the radiative intensity at some position to solve such an equation. We will use a boundary condition to specify the intensity at the wall of the SWATH geometry. To form a boundary condition, we will first look at the interaction of thermal radiation with the wall.

When a radiation beam falls on a wall, the wall can reflect, absorb, or transmit the incoming ray. The walls used in SWATH are of stainless steel, which is opaque to thermal radiation, so there is no transmission. The only interactions that remain are absorption and reflection. Absorptivity α is the probability of absorption, and reflectivity ρ is the probability of reflection. The absorptivity and reflectivity add up to one since the total chance an interaction occurs is one. We can further divide reflection into two types: specular, similar to how a mirror reflects, and diffuse, which reflects light in all directions equally. Specular and diffuse reflection have their reflectivities ρ^s and ρ^d. ρ^s and ρ^d add up to the total reflectivity ρ. Kirchhoff's law states

that the emissivity and absorptivity of a surface are the same [11]. By combining all these facts, we get

$$\varepsilon + \rho^s + \rho^d = 1. \tag{2.12}$$

When the reflectivities of a material are known, the emissivity may be determined using the above equation. The reflectivities of a material can be determined, for instance, by an ultraviolet–visible–near-infrared UV-VIS-NIR spectrophotometer. Figure 2.3 shows the result of such a determination on a stainless steel mirror.

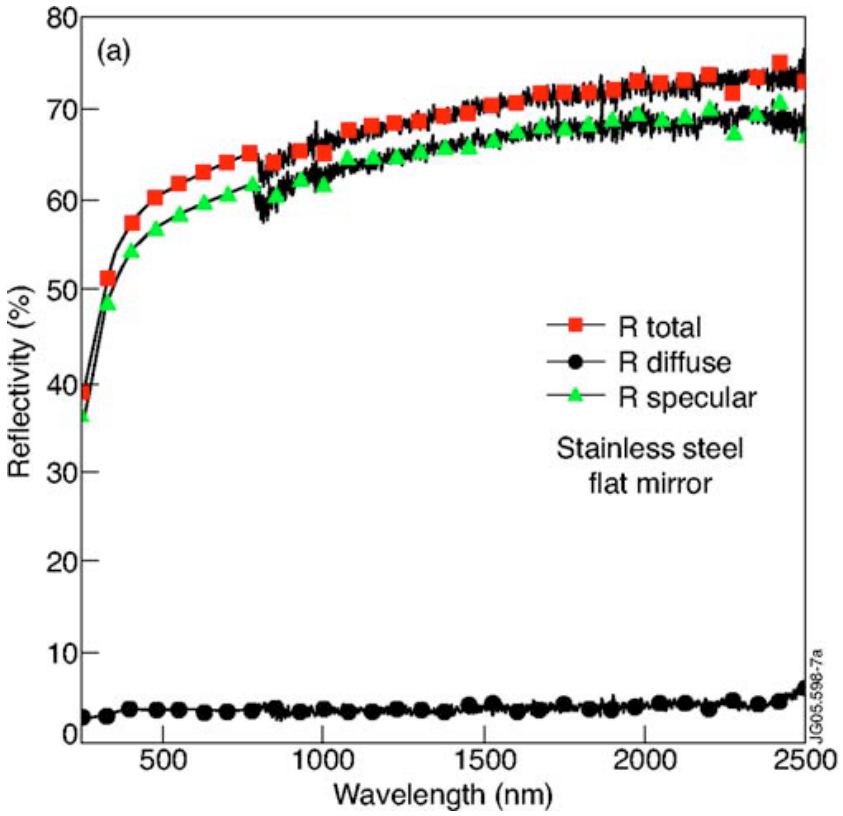

Figure 2.3: The specular and diffuse reflectivities of a stainless steel mirror at different wavelengths [13].

Now that the interactions on the wall have been explained, the boundary condition can be formulated. It consists of three parts: the emission of the boundary, the diffuse reflection, and the specular reflection. These parts are from left to right on the right side of equation 2.13.

$$I(\boldsymbol{r}_w, \hat{\boldsymbol{\Omega}}) = \varepsilon I_b(\boldsymbol{r}_w) + \frac{\rho^d(\boldsymbol{r}_w)}{\pi} \int\limits_{\boldsymbol{n}\cdot\hat{\boldsymbol{\Omega}}'<0} I(\boldsymbol{r}_w, \hat{\boldsymbol{\Omega}}')|\boldsymbol{n}\cdot\hat{\boldsymbol{\Omega}}'|\, d\Omega' + \rho^s(\boldsymbol{r}_w) I(\boldsymbol{r}_w, \hat{\boldsymbol{\Omega}}_s) \tag{2.13}$$

In the above equation $\boldsymbol{r}_w$ is the position of the wall, $\hat{\boldsymbol{\Omega}}'$ the direction of other rays, $\boldsymbol{n}$ is the unit normal of the boundary wall, and $\boldsymbol{\Omega}_s$ is the direction of the specularly reflected beam [12].

2.4. Salt Optical Properties

To solve the RTE, the optical properties of the salt are needed because molten salts are participating media. The unknown properties are the absorption σ_{aE} and scattering σ_{sE} coefficients. These parameters depend on the composition of the salt used in the Molten Salt Reactor. As mentioned in the introduction (1.2), fluoride or chloride salts are used in MSRs. Fluoride salts

tend to have better heat transfer than chloride salts. Fluoride salts also have low neutron absorption cross-sections, chemical stability at high temperatures, and can dissolve actinides which is paramount for molten salt used (in the primary circuit) [14]. The eutectic LiF-NaF-KF (FLiNaK), the transition metal KF-ZrF_4, and eutectic LiF-BeF_2 (FLiBe) are examples of fluoride salts used in MSRs. FLiNaK (a popular choice in the nuclear community [15]) is used in the SWATH experiment, so the other salts mentioned will not be discussed further.

2.4.1. FLiNaK

As mentioned before, FLiNaK is a eutectic salt meaning it has a lower melting temperature than its constituent parts. FLiNaK or LiF-NaF-KF has a eutectic composition of 46.5−11.5−42 mol %. FLiNaK melts (or solidifies) at 454 °C and boils at 1750 °C. The low melting temperature reduces the energy needed to melt the salt, which is a benefit. Other benefits include a high heat capacity,chemical stability at higher temperatures, and low toxicity [14][16]. The structure of FLiNaK can be seen in figure 2.4.

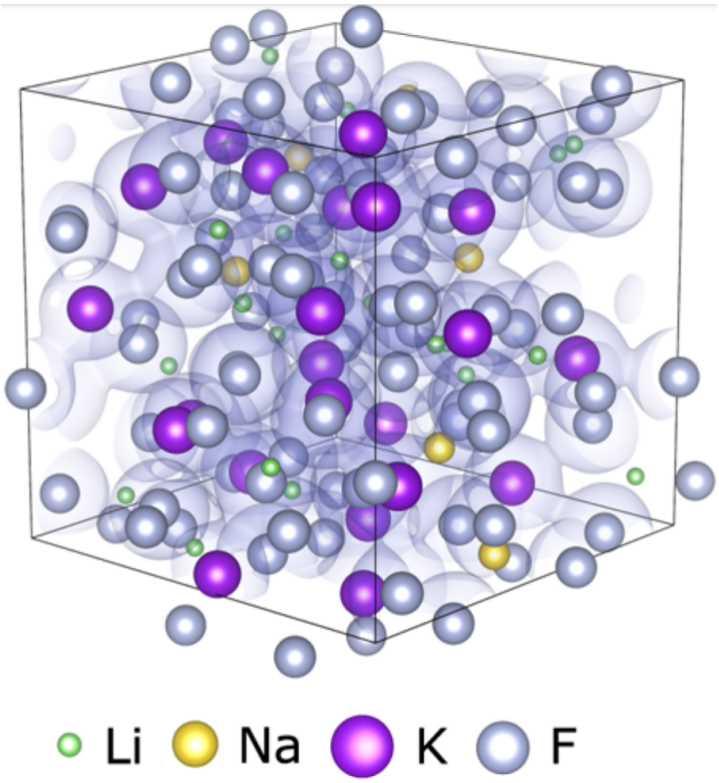

Figure 2.4: The molecular structure of FLiNaK composed of Lithium (Li), Sodium (Na), Potassium (K), and Fluoride (F) molecules [15].

FLiNaK has a high solubility for the actinide fluorides PuF_3, UF_4, and AmF_3 [17]. Because of the previous factor, FLiNaK can be used as a fuel solvent and a coolant salt, although KF has a large parasitic capture cross-section (compared to FLiBe) making it less beneficial as a fuel solvent. The lithium used in FLiNaK has to be at least 99.5% ^{7}Li instead of ^{6}Li because ^{6}Li has a high parasitic neutron capture cross-section. Capture by ^{6}Li can cause a decrease in reactivity inside a reactor due to tritium generation [14].

2.4.2. Absorption Coefficient

Since FLiNaK is a participating medium, there is both scatter and absorption of thermal radiation inside the molten salt. The scattering of thermal radiation will not be included in the simulation model due to its expected negligible value [18]. Radiation is scattered at high energy by interaction with outer shell electrons and drops off rapidly with wavelength. Thermal radiation is predominantly infrared radiation, which has low energy. The scattering of photons will have a negligible effect on thermal radiation. However, the scattering of thermal radiation can become important again when there is a discrete change in the index of refraction n within the salt [18]. This discrete change can happen when there are pollutants in the salt or phase changes. These possibilities causing a change in n are irrelevant in this study since it is assumed there is only pure and entirely molten salt.

Physical Mechanism

The physical mechanism involving the linear absorption coefficient σ_{aE} will first be explained, after which the calculation method and values will be given.

There are three energy regions one can divide the absorption phenomena in. The three regions can be seen in Figure 2.5, The first region is high energy with a short wavelength where electromagnetic radiation, like thermal radiation, may interact with the electronic bands in the molten salt. This interaction is in the form of promoting electrons from orbitals into higher energy states in the valence band or promoting electrons into the conduction band [18]. These effects lead to a high absorption coefficient value in the high-energy region.

The second region is intermediate energy and wavelength, with a low absorption coefficient due to the photons having too little energy to excite electrons across the band gap and being too energetic for low energy absorption. The small amount of absorption that does happen in this region is dominated by scattering losses and impurities in the salt for real-world materials.

The final region is low energy and high wavelength. In this last region, photons can be absorbed by conversion to phonons that are characteristic of vibrational modes of liquid FLiNaK. The phonons can be produced by vibrational modes of the long-range lattice or by local vibration and short-range ordering [18]. The absorption in this region, like the first region, is high.

The shape of the absorption coefficient depends on four phenomena. These effects are Urbach absorption, Brillouin scattering, and Rayleigh scattering at short wavelengths and high energy and multi-phonon absorption at long wavelengths and low energy. Urbach absorption and Brillouin scattering occur due to the interactions of photons with the outer-shell electrons of the atoms in the salt [19]. The region where they determine the shape is called the Urbach tail. However, these two phenomena are unessential due to the Urbach tail not overlapping with the emission spectrum of black bodies in the applicable temperature ranges used in this thesis. The other effect at high energy is Rayleigh Scattering, a phenomenon of elastic scatter of photons travelling through a medium [18]. Since Rayleigh scatter is elastic, unlike Brillouin scatter which is inelastic, it only alters the direction of incoming radiation. The cross-section of Rayleigh scatter inversely scales with the fourth power of wavelength ($\sigma_{\text{Rayleigh}} \propto 1/\lambda^4$), causing it not to be generally observed for wavelengths approximately over 1 micrometre [19]. The effect of Rayleigh scatter is much smaller than Urbach absorption and Brillouin scatter for relatively pure substances with a small amount of impurities, so this effect is also negligible. Finally, the remaining phenomenon is multi-phonon absorption. Multi- or N-phonon absorption occurs when a vibrational mode in a medium corresponds to the energy of an incoming photon, allowing the entire photon to be absorbed and converted to the vibrational energy of a material, which is the same as heat [18]. The number of physically possible vibrational states decreases exponentially with the energy of the vibrational state, so more are available at low energies

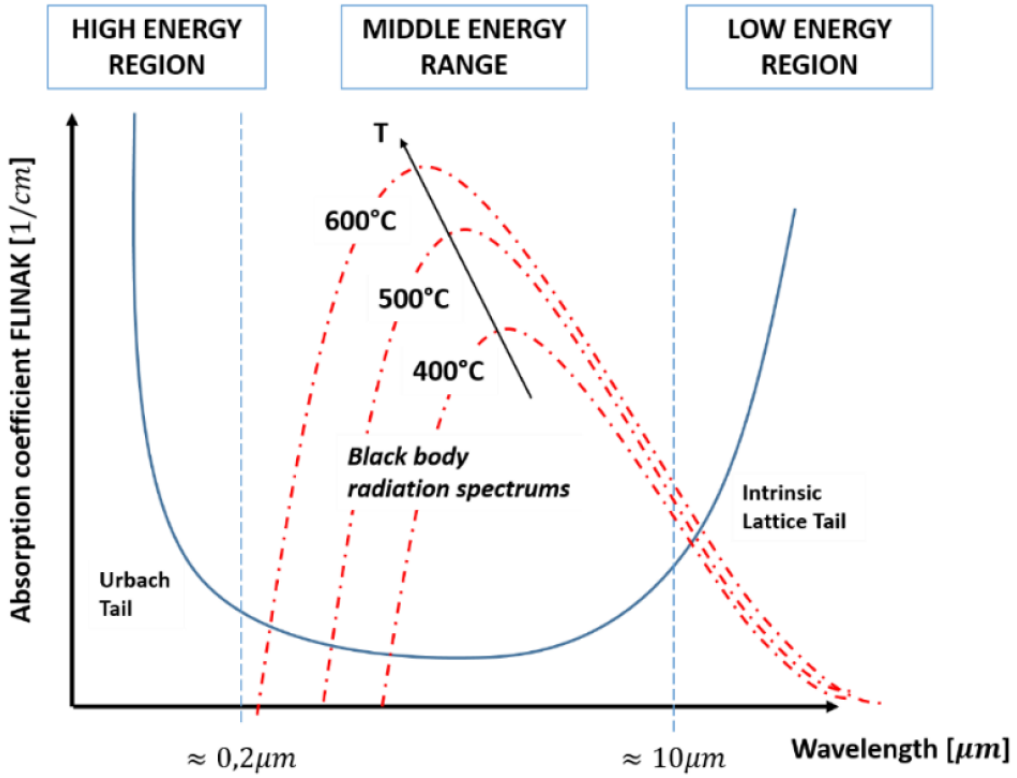

Figure 2.5: Schematic representation of the absorption coefficient for FLiNaK as a function of the wavelength. The black-body radiation spectra for three different temperatures are also represented in the graph [19].

and few at high energies. More available states grant a larger absorption cross-section. The number of states grows exponentially with wavelength, which creates the shape of the intrinsic lattice tail seen in Figure 2.5.

Calculating Coefficient

One way of calculating the absorption coefficient is the method employed in the PhD dissertation of Tano Retamales (2018, [19]). The dissertation used an ab-initio approach using the Quantum ESPRESSO open-source code [20] to calculate the absorption coefficient. This software used Density Functional Theory (DFT) to calculate the phonon frequencies in molten FLiNaK, which were used to determine the (infrared) absorption coefficients. More details about the procedures used can be found in the PhD thesis of Tulip (2004, [21]).

The resulting absorption coefficients calculated by Tano Retamales can be found in Figure 2.6, which also contains the band absorption coefficients. The Urbach tail is not visible in this figure, since absorption coefficient is only given for wavelengths above 3-4 μm, whereas the Urbach trail is present in wavelenghts lower than $\approx 0.2\ \mu m$. The energy spectrum is discretised into groups which is called Multigroup Theory. Multigroup Theory allows more specifications for the various groups, like absorption coefficients or other energy-dependent parameters. The energy spectrum is divided into three groups corresponding to three wavelength divisions: 0-5, 5-10, and 10-∞ micrometres. Converting this to energy gives ∞-0.248, 0.248-0.124, and 0.124-0 electronvolts. The exact values of the band or homogenised absorption coefficients can be found in Table 2.1. The spectral radiative intensity of a black body at 700 K with its banded absorption coefficient is given in Figure 2.7.

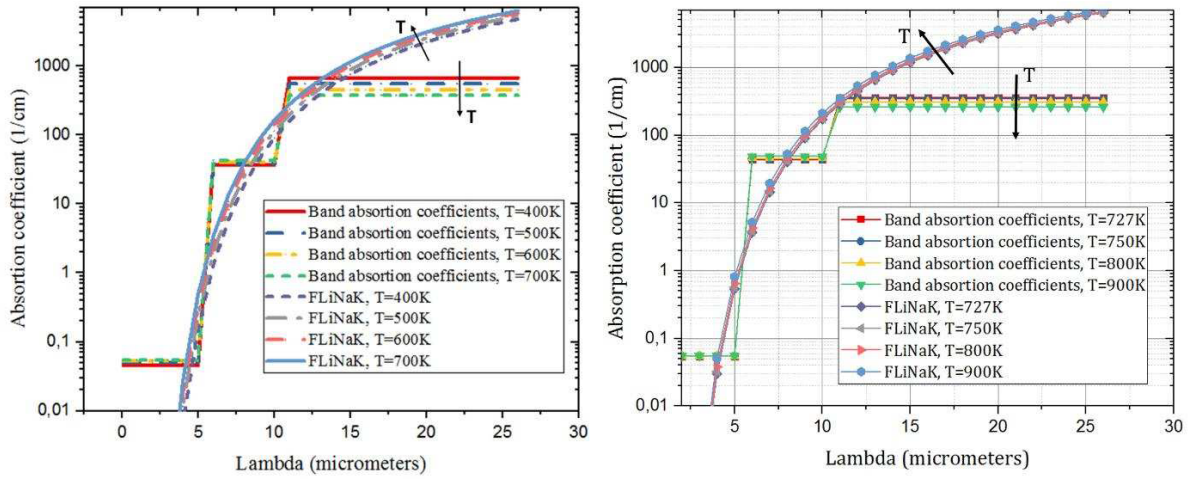

Figure 2.6: Spectral absorption coefficients and homogenised absorption coefficients for the proposed bands for FLiNaK [19]. The values of the homogenised absorption coefficients can be found in Table 2.1.

Table 2.1: Effective absorption coefficients for the bands proposed in FLiNaK as a function of temperature [19].

	400 K	500 K	600 K	700 K	727 K	750 K	800 K	900 K
$\sigma_{a,0-0.124\ \text{eV}}$ (1/cm)	673.1	551.3	453.7	375.7	356.8	341.5	311.1	260.2
$\sigma_{a,0.124-0.248\ \text{eV}}$ (1/cm)	36.8	38.2	40.2	42.9	43.6	44.2	45.7	48.2
$\sigma_{a,0.248-\infty\ \text{eV}}$ (1/cm)	0.046	0.050	0.053	0.055	0.055	0.055	0.055	0.055

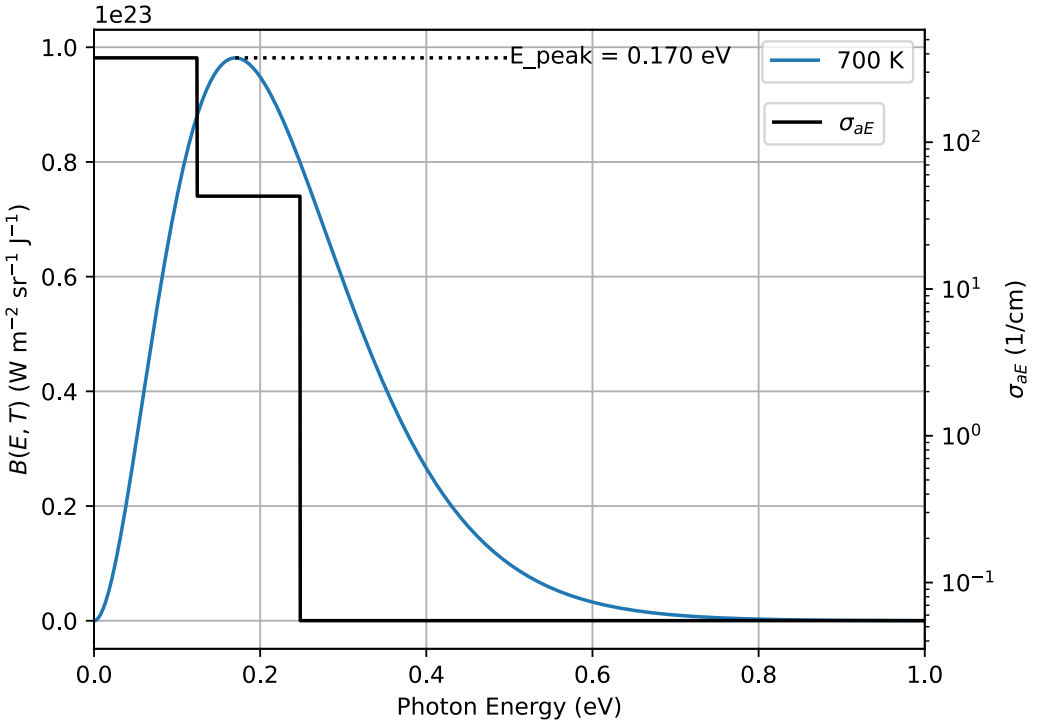

Figure 2.7: Planck's law for black bodies is shown using temperatures of 700 Kelvin with its corresponding effective band absorption coefficient. The photon energy in electron volts is on the horizontal axis, and the corresponding spectral radiative intensity $B_E(E,T)$ is on the left vertical axis. The band absorption coefficient is on the right vertical axis. The photon energy at the maximum spectral irradiance is also visible. The values of the absorption coefficient at 700 K can be found in Table 2.1.

2.5. Radiative Heat Flux

After the radiative intensity, only the corresponding heat flux is left to be determined. The heat flux is the thermal energy flow per area per time. Knowing the thermal energy in a system allows, for example, the power production of an MSR to be calculated and the temperature distribution to be defined. Section 4.2 explains the use of the radiative heat flux in calculating the temperature.

The total heat flux vector can be calculated from the intensity using

$$\boldsymbol{q}_R(\boldsymbol{r}) = \int_0^\infty \int_{4\pi} I_E(\boldsymbol{r}, \hat{\boldsymbol{\Omega}}) \hat{\boldsymbol{\Omega}} \, d\Omega dE, \tag{2.14}$$

with $\boldsymbol{q}_R(\boldsymbol{r})$ the radiative heat flux. As will be seen in Section 4.2, only the divergence of the radiative heat flux is needed to determine the temperature distribution. The divergence of the heat flux can be calculated by

$$\nabla \cdot \boldsymbol{q}_R = \int_0^\infty \sigma_{aE} \left(4\pi B_E - \int_{4\pi} I_E \, d\Omega \right) \, dE. \tag{2.15}$$

Equation 2.15 is derived by integrating the quasi-steady RTE over all solid angles Ω and photon energies E.

3

Discrete Ordinates Method

The Discrete Ordinates Method (DOM), or S_N method, is a numerical technique to discretize angular variables. The S_N method will handle the integration of radiative intensity over solid angles. It does so by splitting the RTE into multiple partial differential equations, each corresponding to a discrete direction from a set spanning the total solid angle of 4π. These discretized angles are called ordinates.

In the discrete ordinates method, an integral over the direction can be replaced with a weighted summation,

$$\int_{4\pi} f(\hat{\boldsymbol{\Omega}})\, d\Omega = \sum_{i=1}^{n} w_i f(\hat{\boldsymbol{\Omega}}_i), \tag{3.1}$$

where f is a function, n is the number of discretized directions, w_i are the quadrature weights, and $\hat{\boldsymbol{\Omega}}_i$ are the discrete directions. Using equation 3.1, we can rewrite the RTE from equation 2.11 into a set of n PDEs,

$$\hat{\boldsymbol{\Omega}}_i \cdot \nabla I_E(\boldsymbol{r}, \hat{\boldsymbol{\Omega}}_i) + \sigma_{tE} I_E(\boldsymbol{r}, \hat{\boldsymbol{\Omega}}_i) = \sigma_{aE} I_{bE}(\boldsymbol{r}) + \frac{\sigma_{sE}}{4\pi} \sum_{j=1}^{n} w_j I_E(\boldsymbol{r}, \hat{\boldsymbol{\Omega}}_j), \qquad i = 1, ..., n, \tag{3.2}$$

with a corresponding rewritten boundary condition as

$$I(\boldsymbol{r}_w, \hat{\boldsymbol{\Omega}}_i) = \varepsilon I_b(\boldsymbol{r}_w) + \rho^s(\boldsymbol{r}_w) I(\boldsymbol{r}_w, \hat{\boldsymbol{\Omega}}_{i,s}) + \frac{\rho^d(\boldsymbol{r}_w)}{\pi} \sum_{\boldsymbol{n}\cdot\hat{\boldsymbol{\Omega}}_j < 0} w_j I(\boldsymbol{r}_w, \hat{\boldsymbol{\Omega}}_j) |\boldsymbol{n} \cdot \hat{\boldsymbol{\Omega}}_j|, \quad \boldsymbol{n} \cdot \hat{\boldsymbol{\Omega}}_i > 0 \tag{3.3}$$

As mentioned in Section 2.4.2 the isotropic scatter σ_{sE} is negligible, so Equation 3.2 reduces to

$$\hat{\boldsymbol{\Omega}}_i \cdot \nabla I_E(\boldsymbol{r}, \hat{\boldsymbol{\Omega}}_i) + \sigma_{tE} I_E(\boldsymbol{r}, \hat{\boldsymbol{\Omega}}_i) = \sigma_{aE} I_{bE}(\boldsymbol{r}), \qquad i = 1, ..., n. \tag{3.4}$$

To apply equations 3.3 and 3.4, we need to know the directions and their complementary weights. One can make sets of directions and weights arbitrarily, but desirable conditions can cause restrictions on the sets used. It is customary to choose completely symmetric (invariant of 90° rotation) sets that also satisfy the zeroth, first, and second moments conditions, which

are

$$\int_{4\pi} d\Omega = 4\pi = \sum_{i=1}^{n} w_i, \tag{3.5}$$

$$\int_{4\pi} \hat{\mathbf{\Omega}}\, d\Omega = \mathbf{0} = \sum_{i=1}^{n} w_i \hat{\mathbf{\Omega}}_i, \tag{3.6}$$

$$\int_{4\pi} \hat{\mathbf{\Omega}}\hat{\mathbf{\Omega}}\, d\Omega = \frac{4\pi}{3}\boldsymbol{\delta} = \sum_{i=1}^{n} w_i \hat{\mathbf{\Omega}}_i \hat{\mathbf{\Omega}}_i, \tag{3.7}$$

where $\boldsymbol{\delta}$ is the unit tensor, which is three by three matrix with ones on the diagonal and zeros otherwise. Apart from the previous conditions, there is an additional condition called the half-moment discussed in Section 3.1. The number of directions and quadrature corresponding weights depend on the N, seen in S_N. N indicates the number of different direction cosines used per principal direction ([$\hat{\boldsymbol{x}}, \hat{\boldsymbol{y}}, \hat{\boldsymbol{z}}$] or [$\hat{\boldsymbol{i}}, \hat{\boldsymbol{j}}, \hat{\boldsymbol{k}}$]). There are a total of $n = N(N+2)$ different directions. Increasing N yields an increased accuracy but raises the computational cost increasingly with every step. Each three-dimensional direction $\hat{\mathbf{\Omega}}_i$ can be expressed by a combination of direction cosines ξ_i, η_i, and μ_i:

$$\hat{\mathbf{\Omega}}_i = (\hat{\mathbf{\Omega}}_i \cdot \hat{\boldsymbol{i}})\hat{\boldsymbol{i}} + (\hat{\mathbf{\Omega}}_i \cdot \hat{\boldsymbol{j}})\hat{\boldsymbol{j}} + (\hat{\mathbf{\Omega}}_i \cdot \hat{\boldsymbol{k}})\hat{\boldsymbol{k}} = \xi_i\hat{\boldsymbol{i}} + \eta_i\hat{\boldsymbol{j}} + \mu_i\hat{\boldsymbol{k}}. \tag{3.8}$$

Figure 3.1 shows different directions by combining direction cosines in an octant. The sum of the squared direction cosines should be equal to one since $\hat{\mathbf{\Omega}}$ is a unit vector, or

$$\xi^2 + \eta^2 + \mu^2 = 1. \tag{3.9}$$

3.1. Half-moment

Besides the symmetry, the zeroth, first, and second moments, another condition will be required for calculating the set of directions and quadrature weights. This additional condition is the half-moment (or half-range moment) which is

$$\int_{\hat{\boldsymbol{n}}\cdot\hat{\mathbf{\Omega}}<0} |\hat{\boldsymbol{n}} \cdot \hat{\mathbf{\Omega}}|\, d\Omega = \pi = \sum_{\hat{\boldsymbol{n}}\cdot\hat{\mathbf{\Omega}}_i>0} w_i \hat{\boldsymbol{n}} \cdot \hat{\mathbf{\Omega}}_i. \tag{3.10}$$

This requirement of integrating over the half-range (or half sphere) is not satisfied using solely the original conditions. The resulting integration seen in equation 3.10 does not equal π when using the original conditions, although the error at higher-order approximations (larger N) is lower but doesn't disappear. Since such an integral is in the boundary condition defined by equation 2.13, the half-moment condition is needed.

A concern about using this half-moment is that this requirement is impossible to satisfy in combination with the original conditions, meaning when $\hat{\boldsymbol{n}} = \hat{\boldsymbol{i}}, \hat{\boldsymbol{j}}$, or $\hat{\boldsymbol{k}}$. The half-moment condition is only satisfied for the principal orientations. Now that all conditions that will be used have been discussed, the quadrature weights and directions can be calculated.

3.2. Quadrature

Now that all conditions have been specified, the discrete directions and their corresponding quadrature weights can be calculated. The symmetry constraint, also called level symmetric,

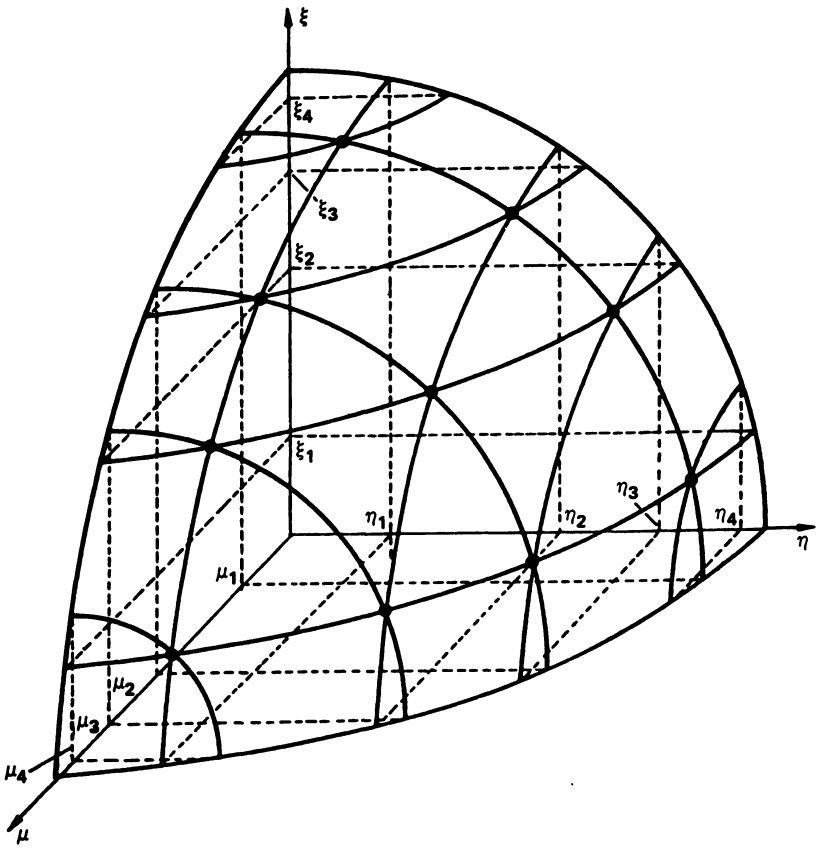

Figure 3.1: A level symmetric S_8 discrete ordinates set [22]. Different directions are shown by points at the intersections of the direction cosines in an octant.

causes the ordinate directions to be invariant to a 90° rotation about any axis. The symmetry condition gives us the following equation:

$$\xi_i = \eta_i = \mu_i \tag{3.11}$$

for all i. Combining this relation with Equation 3.9 gives us:

$$\mu_i{}^2 + \mu_j{}^2 + \mu_k{}^2 = 1, \tag{3.12}$$

where i, j, and k are indices going from 1 to $N/2$ in steps of one. The other $N/2$ direction cosine values are the negative counterparts of the μ_i referenced above. Because of the symmetry, indices i, j, and k sum up to $N/2+2$. So Equation 3.12 can be rewritten as

$$\mu_i{}^2 + \mu_j{}^2 + \mu_{N/2+2-i-j}{}^2 = 1, \tag{3.13}$$

where $i = 1, 2, ..., N/2$ and $j = 1, 2, ..., N/2 - i + 1$. The solution to this problem is

$$\mu_i{}^2 = \mu_1{}^2 + (i-1)C, \qquad i = 1, 2, ..., N/2, \tag{3.14}$$

where

$$C = \frac{2(1 - 3\mu_1{}^2)}{N-2}. \tag{3.15}$$

The μ_i are all fixed except μ_1, so the ordinates depend on the only degree of freedom μ_1. For example, if $N = 2$, there is only one μ_1 choice because Equation 3.12 must hold. So $\mu_1 = 1/\sqrt{3}$ in three dimensions using only symmetric conditions. The quadrature weights of each ordinate also need to be determined. The weights must be rotationally invariant due to the symmetry. Figure 3.2 shows points of equal weight in an octant for different S_N approximations. For instance, an S_4 approximation has equal weights for each of its three ordinates

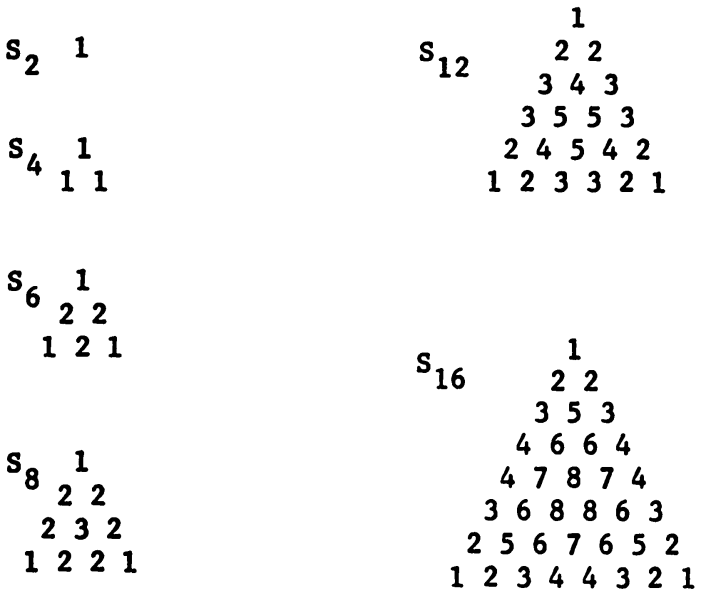

Figure 3.2: Discrete ordinates configuration for one octant showing ordinates of equal weight [22].

per octant, but an S_8 approximation has three weights for its ordinates. Again looking at the S_8 approximation, the sole ordinate in the centre has w_3, the ordinates around the centre have w_2, and the ordinates at the vertices have w_1.

All weights and μ_1 can be determined by matching all half-range moments. The matching is done by solving equations [23]

$$\int_0^1 \mu^i \, d\mu = \frac{1}{i+1} = \sum_{j=1}^{N/2} l_j {\mu_j}^i, \qquad i = 0, 1, ..., N/2, \tag{3.16}$$

where l_j are the level weights. Level weights are the combined ordinate weights of one level. For instance, the S_8 approximation in Figure 3.2 has four level weights: the bottom row $l_1 = 2w_1 + 2w_2$, the lower-middle row $l_2 = 2w_2 + w_3$, the upper-middle row $l_1 = 2w_2$, and the top row $l_1 = w_1$. Solving this system of equations gives negative weights for $N = 12$ or higher. The resulting μ_1 and weights can be found in Table 3.1. Negative weights tend to have higher truncation errors, so an alternate quadrature scheme is used for $N = 12$ and $N = 16$ that is not as accurate, but only gives positive weights. This alternate quadrature scheme does not use Equation 3.16 but instead uses

$$\mu_1 = \frac{(N-2)(1-\sqrt{1-\alpha}) - (N-5)\alpha}{(N-5)^2\alpha - (N-2)(N-8)} \tag{3.17}$$

to find μ_1, where $\alpha = ((4/\pi)^2 - 1)^2$. The other μ_i are again calculated using Equation 3.14. The weights of the alternate quadrature are found by solving

$$\frac{2\sqrt{1-{\mu_j}^2}}{\pi} = \frac{\sum w_i \mu_i}{\sum w_i} \tag{3.18}$$

at each level, where i sums over the weights at level $j = 1, 2, ..., N/2$. For example, in the S_6 approximation, the resulting equations will be

$$w_1\mu_1 + w_2\mu_2 + w_1\mu_3 = (w_1 + w_2 + w_1)\frac{2\sqrt{1-{\mu_1}^2}}{\pi} \tag{3.19}$$

$$w_2\mu_1 + w_2\mu_2 = (w_2 + w_2)\frac{2\sqrt{1-{\mu_2}^2}}{\pi} \tag{3.20}$$

$$w_1\mu_1 = w_1\frac{2\sqrt{1-{\mu_3}^2}}{\pi} \tag{3.21}$$

The last two equations cannot both be satisfied, so the last equation, which has the general form

$$\mu_1 = \frac{2\sqrt{1-{\mu_{N/2}}^2}}{\pi} \tag{3.22}$$

will be discarded. Instead, the discarded equation is replaced by the zeroth moment in Equation 3.5 to solve the system of equations. The results for $N = 12$ and $N = 16$ can be found in Table 3.1.

Table 3.1: Quadrature weights w_i and ordinate direction cosines μ_i for different approximation orders N. The quadrature is (level) symmetric and fulfils the zeroth, first, second, and half (only for principal directions) moments. $N = 12$ and $N = 16$ use an alternate quadrature scheme compared to the second to eighth-order approximations. The second-order approximation is only valid for two-dimensional cases.

Approximation Order N	**Ordinate Direction Cosines** μ	**Weights** w
2 (only 2D)	$1/2$	$w_1 = \pi/2$
4	$\mu_1 = (1 - \sqrt{6}/6)/2$ $\mu_2 = 0.908248290463863$	$w_1 = \pi/6$
6	$\mu_1 = 0.18386710903370068$ $\mu_2 = 0.6950513960188804$ $\mu_3 = 0.908248290463863$	$w_1 = 0.16095181814902979$ $w_2 = 0.36264695744926906$
8	$\mu_1 = 0.14225553242324152$ $\mu_2 = 0.5773502691896258$ $\mu_3 = 0.804008725177561$ $\mu_4 = 0.97955435121792$	$w_1 = 0.17123590548166814$ $w_2 = 0.09922844597569737$ $w_3 = 0.4617179344957074$
12*	$\mu_1 = 0.15965361418676977$ $\mu_2 = 0.4584710575479756$ $\mu_3 = 0.6284124001763655$ $\mu_4 = 0.7613202865953866$ $\mu_5 = 0.8742511154513576$ $\mu_6 = 0.9741773180249087$	$w_1 = 0.981765115221012$ $w_2 = 0.648884514728243$ $w_3 = 0.5393406147308687$ $w_4 = 0.4422147425199504$ $w_5 = 0.3883600881272048$
16*	$\mu_1 = 0.136430525558940$ $\mu_2 = 0.3917822196098881$ $\mu_3 = 0.5370040287564076$ $\mu_4 = 0.6505792389853635$ $\mu_5 = 0.7470832386668413$ $\mu_6 = 0.8324742547341022$ $\mu_7 = 0.9098864786847097$ $\mu_8 = 0.9812101830858783$	$w_1 = 0.7107360601927395$ $w_2 = 0.4543919193213178$ $w_3 = 0.3591154028699344$ $w_4 = 0.32978765463094356$ $w_5 = 0.2944449594145892$ $w_6 = 0.2374684181343291$ $w_7 = 0.2248655941536407$ $w_8 = 0.19721680111237244$

4

Heat Transport

Radiative heat transport is not the only mechanism by which heat gets transported in molten FLiNaK. This chapter will focus on the total heat transport that incorporates the other two heat transport mechanisms: conduction and convection.

4.1. Conduction

The conduction of heat follows Fourier's Law which shows that the heat flux of conduction

$$\boldsymbol{q}_C = -\lambda \nabla T, \tag{4.1}$$

which depends on the thermal conductivity λ and the gradient of temperature T. Thermal conductivity is a material property. The thermal conductivity of FLiNaK was found in the literature ([24], [25]) as having a relation

$$\lambda = 0.36 + 5.6 \cdot 10^{-4} T \pm 0.01 \text{ W m}^{-1} \text{ K}^{-1}, \tag{4.2}$$

which has a value of 0.864 ± 0.01 W m^{-1} K^{-1} at 900 Kelvin. Although the thermal conductivity relation shows an increase with temperature, the article by Rudenko. et al. (2022, [26]) displays a decrease in thermal conductivity with temperature. Due to this disagreeing point and for simplicity, the thermal conductivity will be kept constant at the value of 0.864 W m^{-1} K^{-1}. The actual value of thermal conductivity is still under debate because of the difficulties in measuring thermal conductivity [27].

4.2. Energy Balance

For the temperature field inside the SWATH channel geometry to be determined, the energy conservation balance has to be solved. The temperature field is used for accurately simulating the thermal radiation transport (black-body radiation) and to see the effect of thermal radiation.

The general equation for energy balance in a fluid is

$$\rho \frac{Du}{Dt} = \rho \left(\frac{\partial u}{\partial t} + \boldsymbol{v} \cdot \nabla u \right) = -\nabla \cdot \boldsymbol{q} + p \nabla \cdot \boldsymbol{v} + \mu \Phi + \dot{Q}''', \tag{4.3}$$

where ρ is the density, u is the internal energy, $\boldsymbol{v}$ is the velocity field, $\boldsymbol{q}$ is the total heat flux vector which is equal to the sum of conduction heat flux $\boldsymbol{q}_C$ and radiative heat flux $\boldsymbol{q}_R$, p is the pressure, μ is the viscosity, Φ the dissipation function, and $\dot{Q}'''$ is the heat generated in the medium (like chemical reactions) [12]. The term $\boldsymbol{v} \cdot \nabla u$ represents the transport of internal

energy via convection. Using the following relation of the specific heat capacity at constant volume V:

$$c_v = \left(\frac{\partial u}{\partial T}\right)_V, \tag{4.4}$$

equation 4.3 can be rewritten as

$$\rho c_v \frac{DT}{Dt} = \rho c_v \left(\frac{\partial T}{\partial t} + \boldsymbol{v} \cdot \nabla T\right) = \nabla \cdot (\lambda \nabla T) + p \nabla \cdot \boldsymbol{v} + \mu\Phi + \dot{Q}''' - \nabla \cdot \boldsymbol{q}_R, \tag{4.5}$$

where the heat flux has also been replaced by conduction heat flux $\boldsymbol{q}_C$ and radiative heat flux $\boldsymbol{q}_R$. Equation 4.5 can be further simplified by assuming FLiNaK is an incompressible fuel, meaning that the density ρ is constant, which means the $\nabla \cdot \boldsymbol{v} = 0$ term will become zero due to mass balance (also called the continuity equation) and the specific heat capacity at constant volume c_v can be replaced with the heat capacity at constant pressure c_p. Also, the viscous dissipation term $\mu\Phi$ is presumed to be negligible, and $\dot{Q}'''$ is assumed to be zero. These simplifications give us

$$\rho c_p \left(\frac{\partial T}{\partial t} + \boldsymbol{v} \cdot \nabla T\right) = \lambda \nabla^2 T - \nabla \cdot \boldsymbol{q}_R. \tag{4.6}$$

To solve the above equation for temperature T, the density ρ, the specific heat capacity c_p, and the velocity field $\boldsymbol{v}$ have to be defined. The thermal conductivity λ and the radiative heat flux $\boldsymbol{q}_R$ (Section 2.5) have already been defined.

The density of FLiNaK ρ is temperature dependent, as found in the literature ([15], [25], [28]). Because the density is assumed to be unchanging, the average of the densities found in the literature at 900 Kelvin will be used as the constant value. The density value will be 2028 kg m^{-3}.

The specific heat capacity c_p of FLiNaK is likewise inconsistent across the literature. Again the value will be averaged from values found in the literature ([24], [25]). This results in $c_p = 1.887$ J g^{-1} K^{-1}.

The remaining unknown variable is the velocity field. The SWATH report (2023, [10]) assumes that the flow is fully developed (i.e. Poiseuille flow) before entering the test section, which is the part that will be simulated. The velocity field will be discussed in the following section.

4.3. Inlet Flow

To specify the convective heat transport, the velocity field of the molten FLiNaK inside the channel geometry has to be determined. As mentioned at the end of the previous section, the velocity profile is a Poiseuille flow. The velocity only has a component in the x-direction, which is the direction perpendicular to the plane of the inlet. As mentioned in the SWATH report, a two-dimensional channel would have a velocity profile

$$v_p(y, h) = 6U_A \frac{y}{h}\left(1 - \frac{y}{h}\right), \tag{4.7}$$

where v_p the Poiseuille velocity profile, U_A is the inlet velocity of the plug profile before it fully developed, and h is the height of the channel. The resulting velocity profile can be seen in Figure 4.1.

The three-dimensional velocity profile is similar to the two-dimensional profile because the three-dimensional shape is the combination of two 2D profiles in each direction perpendicular

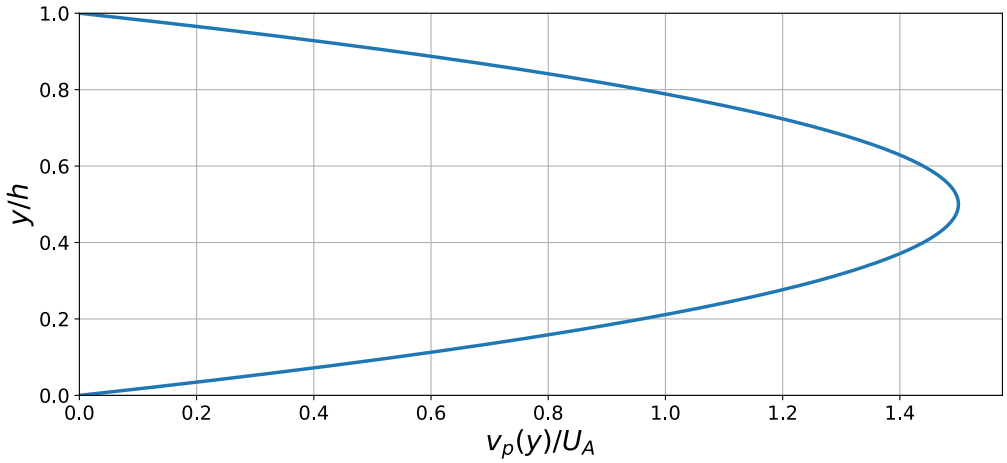

Figure 4.1: The velocity profile v_p of the Poiseuille flow in a two-dimensional channel. The height of the channel is h and U_A is the inlet velocity of the plug profile before it fully developed.

to the inlet. This results in the three-dimensional velocity profile

$$v_x(y,z) = v_p(y,b)v_p(z,a)/U_A = 36U_A\frac{y}{b}\left(1-\frac{y}{b}\right)\frac{z}{a}\left(1-\frac{z}{a}\right). \tag{4.8}$$

There is an additional term $1/U_A$ to conserve the mass balance because the input mass rate of the original plug velocity profile is $\dot{m} = \rho abU_A$, so the mass rate must remain the same. Since it is assumed the density is constant, the volume flow rate $\dot{V} = abU_A$ will also remain constant. The contour profile of Equation 4.8 is shown in Figure 4.2.

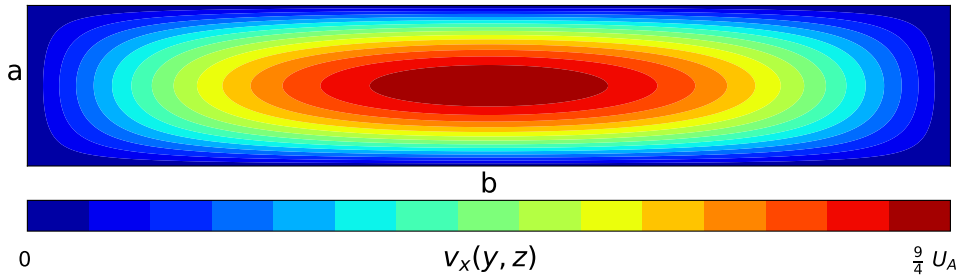

Figure 4.2: The velocity contour of the Poiseuille flow in the channel, where a and b are not to the correct proportion. The 3D Poiseuille flow can be found in Figure A.2.

Now that the velocity profile and the other parameters are known, Equation 4.6 can be solved.

4.4. Finite Volume Method

To numerically solve the simplified energy balance (eq. 4.6), the Finite Volume Method (FVM) will be used. The FVM is a numerical method that does not give the desired temperature field as a continuous value (other numerical methods exist that do give a continuous value). The values of the temperature field is calculated at a finite number of points called grid points. Substituting continuous information with discrete values is called discretization. As the number of grid points becomes very large, the solution of the discretized equation is expected to approach the exact solution of the energy balance [29].

One can divide the calculation domain, the channel geometry in this thesis, into several non-overlapping control volumes centred around each grid point. A schematic drawing of grid points and control volumes in two dimensions can be seen in Figure 4.3. The energy balance will be solved for each of the control volumes (resulting in Equation 4.19). First, the gradient operators in Equation 4.6 will be expanded, which results in

$$\rho c_p \frac{\partial T}{\partial t} + \rho c_p v_x \frac{\partial T}{\partial x} + \rho c_p v_y \frac{\partial T}{\partial y} + \rho c_p v_z \frac{\partial T}{\partial z} = \lambda \frac{\partial^2 T}{\partial^2 x} + \lambda \frac{\partial^2 T}{\partial^2 y} + \lambda \frac{\partial^2 T}{\partial^2 z} - \nabla \cdot \boldsymbol{q}_R. \tag{4.9}$$

From Section 4.3, it is known that only v_x is nonzero, which results in

$$\rho c_p \frac{\partial T}{\partial t} + \rho c_p v_x \frac{\partial T}{\partial x} = \lambda \frac{\partial^2 T}{\partial^2 x} + \lambda \frac{\partial^2 T}{\partial^2 y} + \lambda \frac{\partial^2 T}{\partial^2 z} - \nabla \cdot \boldsymbol{q}_R. \tag{4.10}$$

The above equation is integrated over the timestep Δt and the control volume $\Delta V = \Delta x \Delta y \Delta z$ of grid point $P(i,j,k)$, which gives

$$\begin{aligned} \int_t^{t+\Delta t} \int_{\Delta V} \rho c_p \frac{\partial T}{\partial t}\, dt dV + \int_t^{t+\Delta t} \int_{\Delta V} \rho c_p v_x \frac{\partial T}{\partial x}\, dt dV = \int_t^{t+\Delta t} \int_{\Delta V} \lambda \frac{\partial^2 T}{\partial^2 x}\, dt dV \\ + \int_t^{t+\Delta t} \int_{\Delta V} \lambda \frac{\partial^2 T}{\partial^2 y}\, dt dV + \int_t^{t+\Delta t} \int_{\Delta V} \lambda \frac{\partial^2 T}{\partial^2 z}\, dt dV - \int_t^{t+\Delta t} \int_{\Delta V} \nabla \cdot \boldsymbol{q}_R\, dt dV. \end{aligned} \tag{4.11}$$

The length of the control volume in the x-direction is Δx, and the y- and z-direction have the length Δy and Δz, respectively. The radiative heat flux term $-\nabla \cdot \boldsymbol{q}_R$ will be treated as a source S. After integrating over the control volume and integrating the source and transient term over time, the equation becomes

$$\begin{aligned} &\rho c_p \left(T_P^1 - T_P^0\right) \Delta V + \rho c_p \int_t^{t+\Delta t} \left[(v_x T)_{x^+} - (v_x T)_{x^-}\right] \Delta y \Delta z\, dt = \bar{S} \Delta V \Delta t + \\ &\lambda \int_t^{t+\Delta t} \left[\left(\frac{\partial T}{\partial x}\right)_{x^+} - \left(\frac{\partial T}{\partial x}\right)_{x^-}\right] \Delta y \Delta z + \left[\left(\frac{\partial T}{\partial y}\right)_{y^+} - \left(\frac{\partial T}{\partial y}\right)_{y^-}\right] \Delta x \Delta z + \left[\left(\frac{\partial T}{\partial z}\right)_{z^+} - \left(\frac{\partial T}{\partial z}\right)_{z^-}\right] \Delta x \Delta y\, dt. \end{aligned} \tag{4.12}$$

Here T_P^0 is the temperature of grid point $P(i,j,k)$ at time t, T_P^1 is the temperature of $P(i,j,k)$ at time $t + \Delta t$, $\bar{S}$ is the average value of S over the control volume of point $P(i,j,k)$, and x^+ represents the side of the control volume in the x-direction which is greater than the x-coordinate of point $P(i,j,k)$. Similarly x^- represents the side of the control volume in the x-direction which is smaller than the x-coordinate of point $P(i,j,k)$. The y- and z-direction have the same notation as the x-direction.

Upwind scheme

While the temperature is specified on the grid points, the temperature on the surfaces of the control volume is not yet defined. These undefined temperatures will be given a value using the upwind scheme, alternatively called the upwind-difference scheme or the upstream-difference scheme. Instead of taking the average between grid point $P(i,j,k)$ and its adjacent grid point

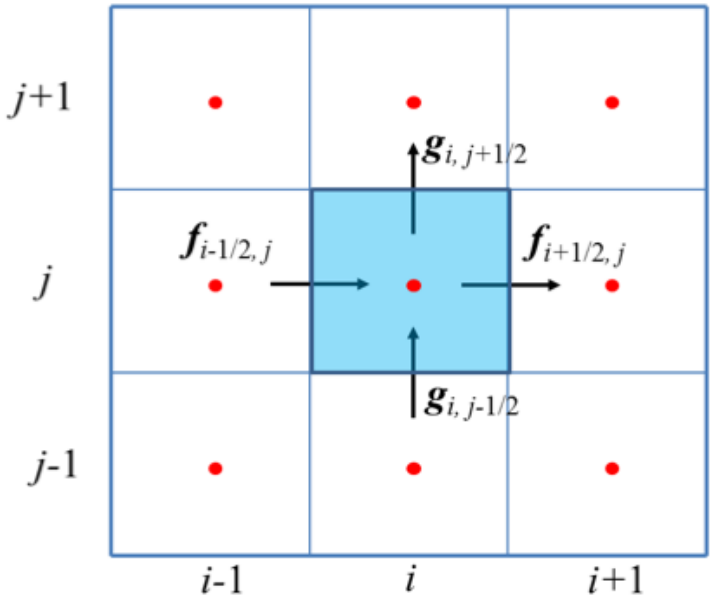

Figure 4.3: Two-dimensional finite-volume mesh [30]. It shows grid points as red dots, the centre control volume is coloured blue, and the arrows denote inflow and outflow into the control volume.

$P(i \pm 1, j, k)$ (in the x-direction), the convection term will use that the temperature value T at the boundary surface equals the upwind side of the boundary. Thus,

$$T_{x^+} = T_{P(i,j,k)} \qquad \text{if} \qquad v_x > 0, \tag{4.13}$$

$$T_{x^+} = T_{P(i+1,j,k)} \qquad \text{if} \qquad v_x < 0. \tag{4.14}$$

Since v_x is presumed to be always positive, $T_{x^+} = T_{P(i,j,k)}$ and $T_{x^-} = T_{P(i-1,j,k)}$. $T_{P(i,j,k)}$ will continue to be written as T_P, and $T_{P(i\pm1,j,k)}$ be as $T_{P\pm\Delta x}$, etc. Applying this to Equation 4.12 gives

$$\begin{aligned}
\rho c_p \left(T_P^1 - T_P^0\right) \Delta V + \rho c_p v_x \int_t^{t+\Delta t} \left(T_P - T_{P-\Delta x}\right) \Delta y \Delta z \, dt = \bar{S} \Delta V \Delta t \\
+ \lambda \int_t^{t+\Delta t} \left[\left(\frac{T_{P+\Delta x} - T_P}{\Delta x}\right) - \left(\frac{T_P - T_{P-\Delta x}}{\Delta x}\right)\right] \Delta y \Delta z \, dt \\
+ \lambda \int_t^{t+\Delta t} \left[\left(\frac{T_{P+\Delta y} - T_P}{\Delta y}\right) - \left(\frac{T_P - T_{P-\Delta y}}{\Delta y}\right)\right] \Delta x \Delta z \, dt \\
+ \lambda \int_t^{t+\Delta t} \left[\left(\frac{T_{P+\Delta z} - T_P}{\Delta z}\right) - \left(\frac{T_P - T_{P-\Delta z}}{\Delta z}\right)\right] \Delta x \Delta y \, dt.
\end{aligned} \tag{4.15}$$

Explicit Time Scheme

The integral over time in Equation 4.15 is yet to be discretized. An assumption needs to be made about how the temperature of T_P changes with time. Many assumptions exist, of which some can be generalized by proposing

$$\int_t^{t+\Delta t} T_P \, dt = \left[f T_P^1 + (1-f) T_P^0\right] \Delta t, \tag{4.16}$$

where f is a weighting factor between 0 and 1 [29]. Specific values of F correspond to well-known schemes like the explicit scheme ($f = 0$), the Crank-Nicolson scheme ($f = 0.5$), and the fully implicit scheme ($f = 1$). The explicit scheme will be used, which modifies Equation 4.16 to

$$\int_{t}^{t+\Delta t} T_P \, dt = T_P^0 \, \Delta t. \tag{4.17}$$

Applying the explicit scheme to Equation 4.15 gives

$$\rho c_p \left(T_P^1 - T_P^0\right) \Delta V + \rho c_p v_x \left(T_P^0 - T_{P-\Delta x}^0\right) \Delta y \Delta z \Delta t = \bar{S} \Delta V \Delta t + \lambda \left(\frac{T_{P+\Delta x}^0 - 2T_P^0 + T_{P-\Delta x}^0}{\Delta x}\right) \Delta y \Delta z \Delta t$$
$$+ \lambda \left(\frac{T_{P+\Delta y}^0 - 2T_P^0 + T_{P-\Delta y}^0}{\Delta y}\right) \Delta x \Delta z \Delta t + \lambda \left(\frac{T_{P+\Delta z}^0 - 2T_P^0 + T_{P-\Delta z}^0}{\Delta z}\right) \Delta x \Delta y \Delta t, \tag{4.18}$$

which can be divided by $\Delta V \Delta t$ to result in

$$\rho c_p \left(\frac{T_P^1 - T_P^0}{\Delta t} + v_x \frac{T_P^0 - T_{P-\Delta x}^0}{\Delta x}\right) = \bar{S}$$
$$+ \lambda \left(\frac{T_{P+\Delta x}^0 - 2T_P^0 + T_{P-\Delta x}^0}{\Delta x^2} + \frac{T_{P+\Delta y}^0 - 2T_P^0 + T_{P-\Delta y}^0}{\Delta y^2} + \frac{T_{P+\Delta z}^0 - 2T_P^0 + T_{P-\Delta z}^0}{\Delta z^2}\right). \tag{4.19}$$

Although using the explicit scheme makes calculating T_P^1 unrelated to other unknowns like $T_{P\pm\Delta x}^1$, it has a serious limitation. The timestep, due to conduction, can not be arbitrarily chosen. The condition for the time step (regarding conduction) is

$$\Delta t < \frac{\rho c_p \Delta V}{2\lambda} \left(\frac{1}{\Delta x^2} + \frac{1}{\Delta y^2} + \frac{1}{\Delta z^2}\right)^{-1}. \tag{4.20}$$

There is also a necessary convergence condition on the timestep involving convection brought upon by the Courant-Friedrichs-Lewy condition, which states that

$$\Delta t \left(\frac{v_x}{\Delta x} + \frac{v_y}{\Delta y} + \frac{v_z}{\Delta z}\right) \leq 1, \tag{4.21}$$

or

$$\Delta t \leq \frac{\Delta x}{v_x} \tag{4.22}$$

since only v_x is nonzero.

If there is a steady-state assumption, the temperature should not change with time, meaning $T_P^1 = T_P^0$, so $T_P^1 - T_P^0 = 0$. This simplifies Equation 4.19 a little to

$$\rho c_p v_x \frac{T_P^0 - T_{P-\Delta x}^0}{\Delta x} = \bar{S}$$
$$+ \lambda \left(\frac{T_{P+\Delta x}^0 - 2T_P^0 + T_{P-\Delta x}^0}{\Delta x^2} + \frac{T_{P+\Delta y}^0 - 2T_P^0 + T_{P-\Delta y}^0}{\Delta y^2} + \frac{T_{P+\Delta z}^0 - 2T_P^0 + T_{P-\Delta z}^0}{\Delta z^2}\right). \tag{4.23}$$

5

Simulation Model

This chapter will discuss the simulation model, expand on the implementation methods used, and the tests performed to see if the implementation methods were successful. Firstly an overview of the model geometry is given, after which implementation methods are discussed, and lastly, some simulation parameters are given.

5.1. Geometry

As mentioned in the introduction (Section), the Flat Channel geometry used in the SWATH facility will be simulated. But instead of the realistically accurate geometry seen in Figure 5.1a, a simplified model is used for the simulation seen in Figure 5.1b to decrease the computational cost. The pertinence of the simplified model was justified by the fact that the diffuser at the inlet (seen in Figure 1.4) ensures that the flow is fully developed in Region B of the Flat Channel test section, making it unnecessary to model the full section geometry [10].

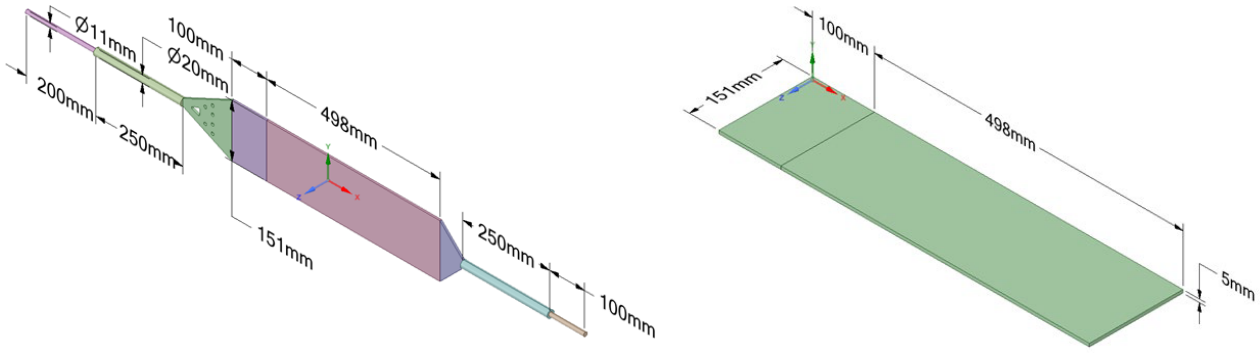

(a) Detailed model with the exact Flat Channel geometry.

(b) Simplified model using a two plates geometry.

Figure 5.1: Geometries of the detailed and the simplified models of the Flat Channel test section [10].

Region B is one of two regions in the manner the channel is divided, with the other being Region A. This division can be seen in Figure 5.2. Region A is the part of the channel that has with $0 \leq x < 0.1$ m and Region B is the part with $0.1 \leq x \leq 0.6$ m. The molten FLiNaK enters the inlet at the entrance of Region A (shaped as the Poiseuille flow seen in Section 4.3). The flow exits at the outlet at the end of Region B. Region A has a length of $L_A = 10$ cm, and all walls in this section are isothermal. The temperature of the walls in Region A, $T_{\text{w,A}}$, is the same as the inlet temperature of the inflowing salt, T_{in}. Region B has thermally insulated

walls, except for the lower wall, which has a fixed temperature $T_{\text{w2,B}}$ that is higher than the inlet temperature. Region B has a length of $L_B \approx 50$ cm. The height of the channel is $a = 0.5$ cm, and the width is $b \approx 15$ cm.

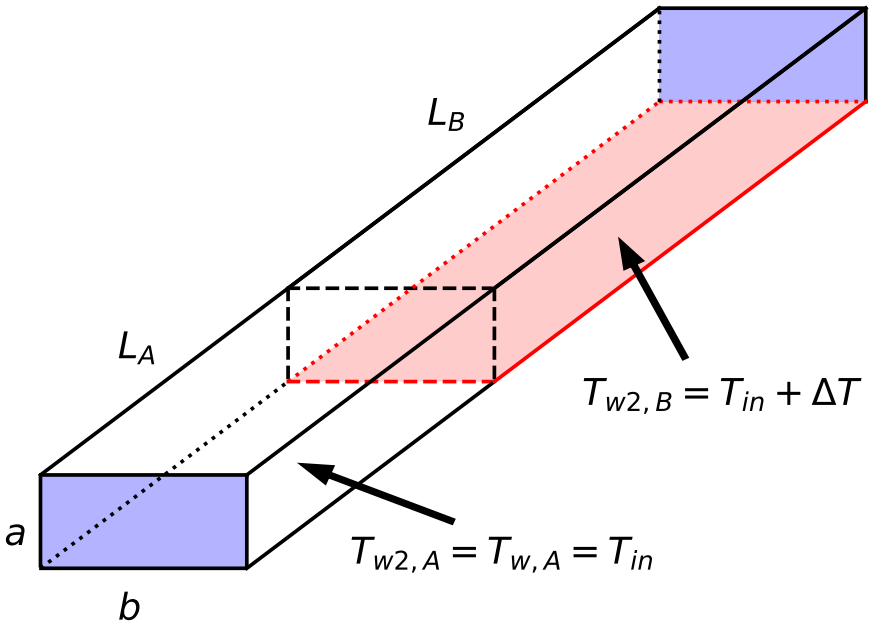

Figure 5.2: A schematic drawing of the simplified flat channel. Red indicates a heated wall at constant temperature, the blue indicate the in- and output of the channel, and white walls are adiabatic.

5.2. Implementation

In the simulation, two different models work together: the radiation and heat models. The radiation model simulates the transport of thermal radiation by solving the RTE (eq. 2.11) using the DOM, resulting in the heat flux from thermal radiation. The heat model solves the energy balance (eq. 4.6) using the FVM, resulting in the temperature distribution.

The temperature distribution is necessary to calculate the black-body radiation (Section) used in the radiation model. Conversely, the heat flux from thermal radiation is needed in the heat model. The models are two-way coupled due to the radiative heat flux and the temperature distribution. The two models will be solved alternately while using the latest result of the other model. The initial temperature distribution is uniform, with the same temperature at the inlet, except at the lower wall in Region B, which has its specific temperature.

The following two sections will expand on the workings of the radiation and heat models.

5.2.1. Radiation Model

Apart from dividing the Flat Channel geometry into grid points, the energy of the photons and the angles are also divided or discretized. As seen in Section 2.4.2, the energy of the

photons emitted due to black-body radiation is divided into three energy groups. This is useful because photons of different have different absorption coefficients. The three groups are 0 to 1.23984198, 1.23984198 to 2.47968397, and 2.47968397 to 5 eV. The spectral radiative intensity B_E, seen in Equation 2.2, is integrated over an energy group to get the radiative intensity in a group g, with energy bounds E_1 and E_2:

$$\int_{E_1}^{E_2} B_E(E,T)\,dE. \tag{5.1}$$

Unfortunately, this integral is difficult to solve analytically. The analytical solution of the indefinite integral is

$$\int B_E(E,T)\,dE = \frac{2}{h^3c^2\beta}(E^3\log(1-e^{-\beta E}) - 3E^2/\beta\mathrm{Li}_2(e^{-\beta E}) - 6E\beta^{-2}\mathrm{Li}_3(e^{-\beta E}) - 6\beta^{-3}\mathrm{Li}_4(e^{-\beta E})), \tag{5.2}$$

where $\beta = 1/K_bT$ and Li_s are polylogarithms, which are defined as

$$\mathrm{Li}_s(z) = \sum_{k=1}^{\infty}\frac{z^k}{k^s}\,. \tag{5.3}$$

Instead of solving the radiative intensity in a group analytically, it is solved numerically using the Gauss-Legendre quadrature. To ascertain if this approach is valid, the Gauss-Legendre quadrature was used (using 33 sample points) to integrate the spectral radiative intensity B_E over 0 to a cutoff energy E_c. The result was compared with the analytical integral over the whole energy domain

$$\int_0^{\infty} B_E(E,T)\,dE = \int_0^{\infty}\frac{2}{h^3c^2}\frac{E^3}{e^{E/k_BT}-1}\,dE = \frac{2}{h^3c^2}(k_BT)^4\int_0^{\infty}\frac{x^3}{e^x-1}\,dx = \frac{2\,(k_BT)^4}{h^3c^2}\frac{\pi^4}{15}. \tag{5.4}$$

This comparison can be seen in Figure 5.3, where the relative error is defined as

$$\text{relative error} = f(E_c) = \frac{\int_0^{\infty} B_E(E,T)\,dE - \left[\int_0^{E_c} B_E(E,T)\,dE\right]_{\text{Gauss-Legendre}}}{\int_0^{\infty} B_E(E,T)\,dE}. \tag{5.5}$$

Figure 5.3 show a high error at energies near 1-2 eV, which is logical since Figure 2.1 shows that most of the thermal radiation emitted for the temperature ranges used in the SWATH experiment is done by photons with energies lower than 1 eV, so the error with the total emitted intensity should be the highest. As the cutoff energy increases, the relative error should also decrease since more of the emission spectrum is integrated, thus nearing the value of integrating the whole spectrum. However, this is not the case because the relative error begins growing around 10 eV. This growth indicates an error with the quadrature method, implying that the integration should not be done with an upper bound higher than 10 eV to avoid errors. Analytically, it can be calculated at which cutoff energy E_c most of the radiative intensity is emitted. All but one-millionth part (10^{-6}) of the total emitted intensity is radiated before cutoff energy $22k_BT$. So, it is desirable to choose an upper bound above $22k_BT$ and below 10 eV. Using a temperature of 1000 K, $22k_BT \approx 1.9$ eV Using this info, a cutoff energy E_c or upper

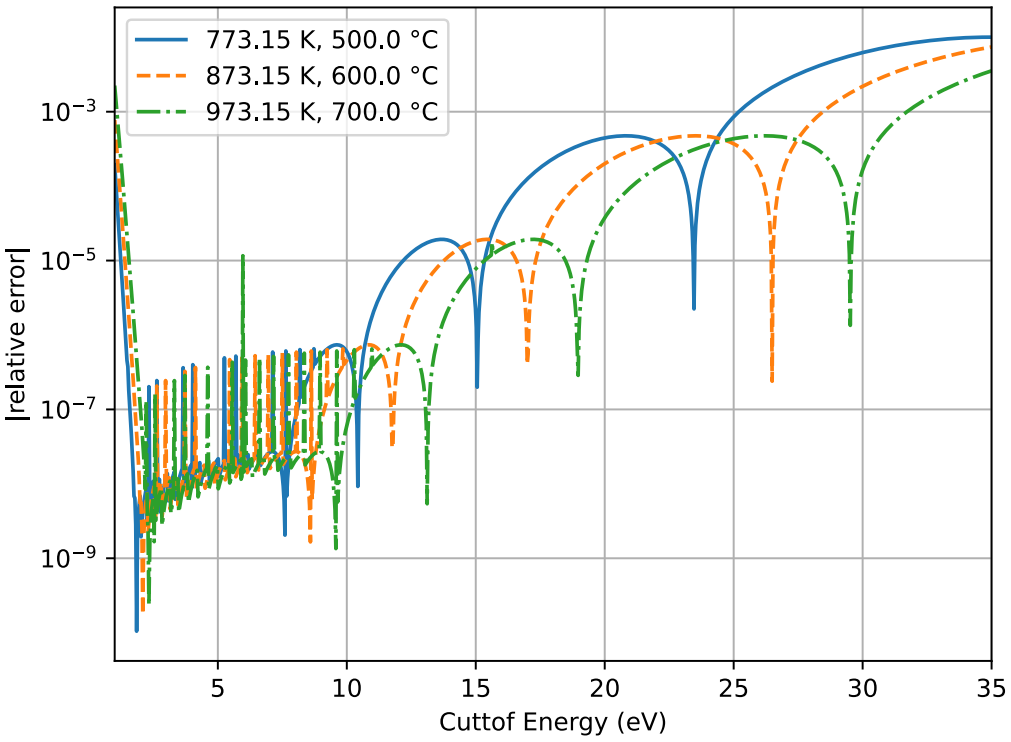

Figure 5.3: The relative error from integrating the black-body spectrum with Gauss-Legendre quadrature. The relative error on the vertical axis is defined in Equation 5.5 and the cutoff energy is on the horizontal axis in electron volts.

bound of 5 eV was chosen, and the spectral radiative intensity above this value is taken as zero.

As mentioned earlier in this section, the angles are discretised according to the method of discrete ordinates. For each ordinate direction, the radiation model sweeps through the mesh elements in the direction of thermal radiation. A possible issue with this method occurs at the boundary. Equation 3.3 shows that radiation from all incoming directions is used in the boundary conditions, but since the diffuse reflectivity is small, the effect of sweeping should also be small.

The boundary conditions in the radiation model are the same at the four walls, the inlet, and the boundary. It emits thermal radiation while also specularly and diffusely reflecting incoming thermal radiation.

5.2.2. Heat Model

The heat model is solved using the FVM and assuming steady state conditions. Also, the heat model uses the same mesh as the radiation model. While the radiation model has only one boundary condition, the heat model has three distinct boundary conditions coming in two types: Neumann and Dirichlet. The inlet, outlet, and all walls in Region B, apart from wall 2, have Neumann boundary conditions where $\frac{\partial T}{\partial z} = \frac{\partial T}{\partial y} = \frac{\partial T}{\partial x} = 0$. The $\frac{\partial T}{\partial z} = \frac{\partial T}{\partial y} = \frac{\partial T}{\partial x} = 0$ is equivalent to adiabatic boundary conditions. Wall 2 in Region B has a Dirichlet boundary condition of $T_{\text{wall}} = T_{\text{in}} + \Delta T$. All walls in region A also have a Dirichlet boundary condition but with a value of T_{in}. With these boundary conditions, the temperature field is calculated using the Gauss-Seidel method. A heuristic-based convergence criterion is used.

5.3. Simulation Parameters

5.3.1. Mesh

As mentioned in the previous section, the radiation and heat models use the same mesh. The mesh is made out of similar-sized hexahedrons. The nodes in each direction are the same. An example of such a mesh can be seen in Figure 5.4.

5.3.2. Parameters

The flat channel geometry will be simulated with different inlet temperatures, volumetric flow rates, and wall temperatures. The unchanging parameters used in the simulation can be found in Table 5.1, and the variable input parameters can be found in Table 5.2. The inlet temperatures 525, 550, 575, and 600 are the temperatures used in the SWATH experiment ([10]). Similarly, the flow rates 0.5, 1.0, and 2.0 are values possible in the SWATH experiment. The flat channel geometry will be simulated with different inlet temperatures, volumetric flowrates, and wall temperatures

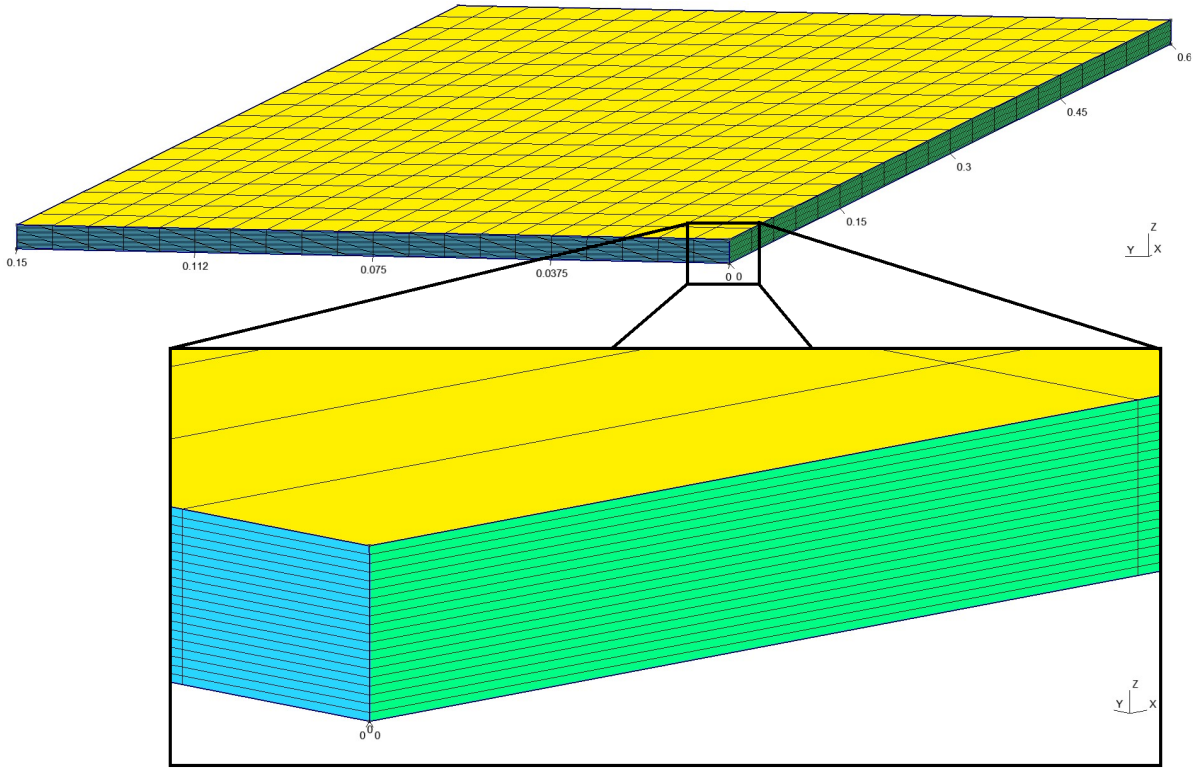

Figure 5.4: A hexahedral mesh of the flat channel geometry used in the radiation and heat model.

Table 5.1: Fixed parameters used in the simulations.

FLiNaK Properties	ρ (kg m^{-3})	2028.0
	λ (W m^{-1})	0.864
	c_p (J g^{-1} K^{-1})	1.887
Channel parameters	L_A (m)	0.1
	L_B (m)	0.5
	a (m)	0.005
	b (m)	0.15
	ε	0.50
	ρ^s	0.45
	ρ^d	0.05

Table 5.2: Variable input parameters used in the simulations.

T_{in} (°C)	Flow rate $\dot{V}$ (L/min) or U_A (m/s)	ΔT (°C)
525	0.5 or 0.01111	25
550	1.0 or 0.02222	50
575	2.0 or 0.04444	100
600	0.045 or 0.001	
700	0.225 or 0.005	
1000		

6

Results and Discussion

In this chapter, the results of the simulation are displayed and discussed, but first, a mesh independence study is performed. The results focus on the temperature profile of the upper wall (or wall 1) of the flat channel geometry. The results will show the impact of heat transfer of thermal radiation by comparing it with the same case when there is only convection and conduction. Also, the effects of the inlet velocity, inlet temperature, and the temperature difference between the upper and lower walls (walls 1 and 2) are presented.

6.1. Mesh Independence Study

Before the simulations will be made, a mesh has to be chosen. This choice is made using a mesh independence study. The simulation will performed with an inlet velocity $v_{\text{in}} = 0.01111$ m/s, inlet temperature $T_{\text{in}} = 525$ °C, and a temperature difference of $\Delta T = 100$ °C. The simulation will be done for five different meshes with different numbers of elements. The shape and proportions of the elements remain the same, but only the size of the elements changes. The meshes will have 6, 12, 18, 24, or 30 nodes in the x, y, and z directions. Respectively, this results in meshes with 216, 1728, 5832, 13824, and 27000 mesh elements. Figures 6.1, 6.2, 6.3, 6.4, and 6.5 show the normalised temperature

$$\frac{T(x,y,z) - T_{\text{in}}}{\Delta T} \tag{6.1}$$

along lines on the edges of the mesh. Some of these lines travel along the x, y, or z axis to determine the mesh dependence in that direction.

The first line the different-sized meshes are compared at is the centre line in the x-direction of the upper wall, which can be seen in Figure 6.1. In this figure, the smallest-sized mesh deviates the most from the other three, which makes sense because higher amounts of mesh elements are more accurate. The second-smallest mesh is closer to the three larger meshes but is still not as accurate. The 5832, 13824, and 27000 element meshes give a similar result on the upper wall of the flat channel, which implies their suitability to be used in the simulation.

The second line seen in Figure 6.2 is similar to the first one but is on the lower wall (which has a constant temperature) instead of the upper. Again, the two smallest-sized meshes deviate from the three larger-sized meshes. The combination of the results obtained from Figures 6.1 and 6.2 shows that only the largest three meshes are accurate enough in portraying the behaviour of temperature changes in the x-direction.

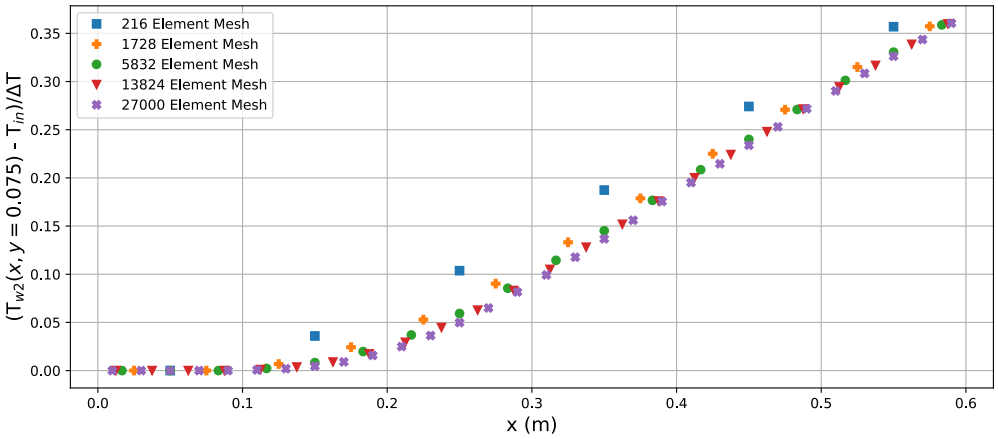

Figure 6.1: The normalised temperature of the elements on the centre line of wall 1 is shown on the vertical axis and the x-coordinate on the horizontal axis. The elements of five different meshes can be seen. The centre line is at $y = 0.075$ m.

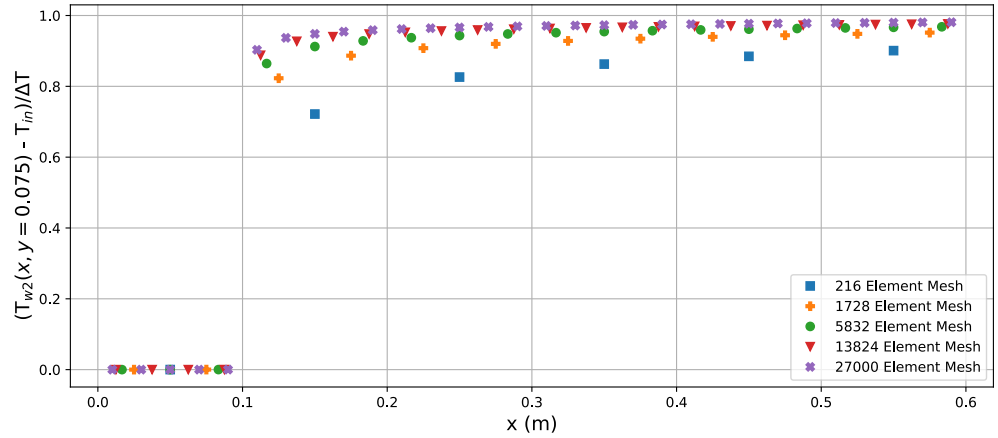

Figure 6.2: The normalised temperature of the elements on the centre line of wall 2 is shown on the vertical axis and the x-coordinate on the horizontal axis. The elements of five different meshes can be seen. The centre line is at $y = 0.075$ m.

The third line where the meshes are compared is the line in the middle of the inlet of the flat channel, dividing the inlet into identically sized upper and lower halves. The temperature should have uniform temperature T_{in} over the whole region, causing the normalized temperature to be zero. Figure 6.3 shows the third line. In this figure, all meshes, apart from the smallest mesh, are equal to zero, as expected.

The fourth line seen in Figure 6.4, which is similar to the third line, is on the outlet of the flat channel. Here, similar results comparable to the first and second lines are seen because the two smallest meshes are inaccurate compared to the three larger ones. The third and fourth lines show that, once again, only the largest three meshes are accurate enough in portraying the behaviour of temperature changes, but this time in the y-direction.

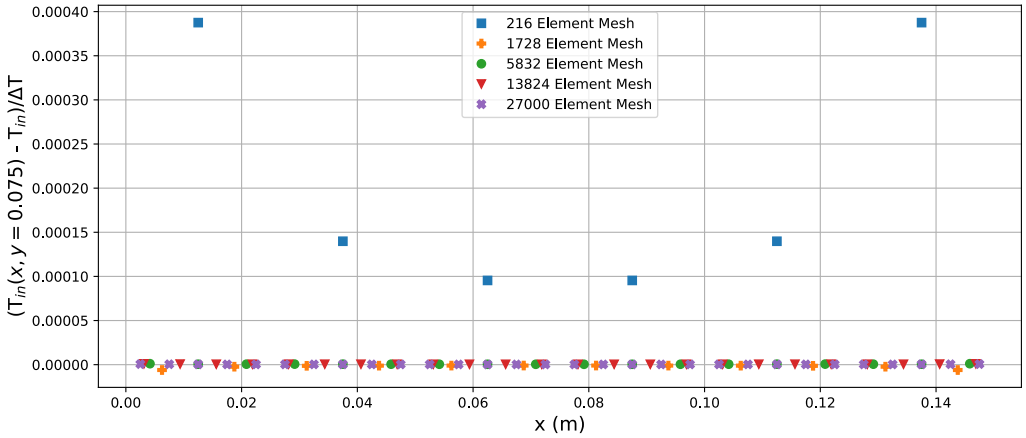

Figure 6.3: The normalised temperature of the elements on the middle line of the input is shown on the vertical axis and the y-coordinate on the horizontal axis. The elements of five different meshes can be seen. The middle line is at $z = 0.0025$ m.

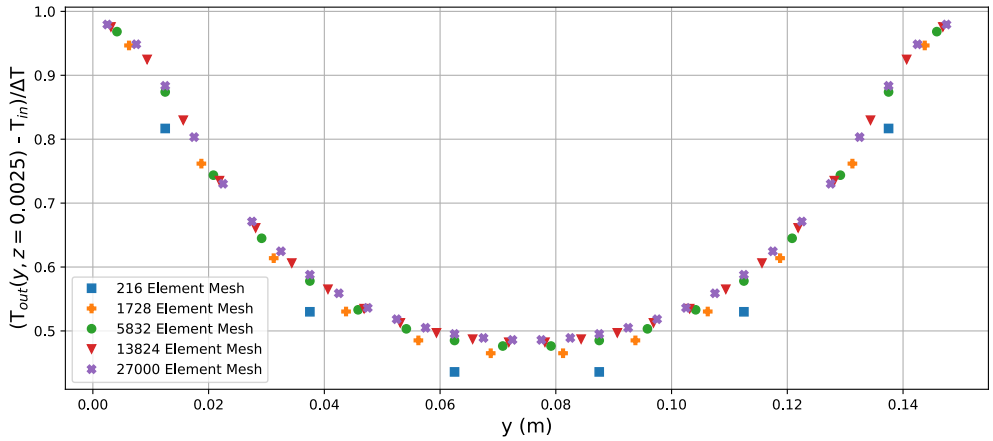

Figure 6.4: The normalised temperature of the elements on the middle line of the output is shown on the vertical axis and the y-coordinate on the horizontal axis. The elements of five different meshes can be seen. The middle line is at $z = 0.0025$ m.

The final line is on the side of the channel. Since the flat channel geometry and its boundary

conditions are symmetrical in the $y = b/2$ plane, lines on either side show the same results. So, only one line will be shown to determine the behavioural changes in the z-direction. The final line is in the middle of the side of the channel, going straight from the bottom wall to the top wall of the channel. This line can be seen in Figure 6.5. The different-sized meshes all lay on the same line, indicating a good description of the temperature behaviour in the z-direction can be achieved by any of these five meshes.

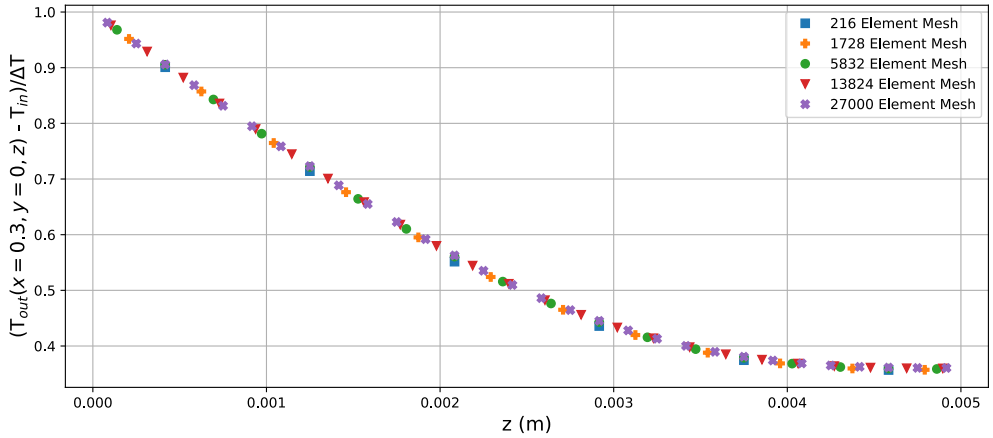

Figure 6.5: The normalised temperature of the elements on the centre line of one side is shown on the vertical axis and the z-coordinate on the horizontal axis. The elements of five different meshes can be seen. The centre line is at $x = 0.3$ m.

From these five meshes, the smallest two meshes are inadequate in modelling the Flat Channel geometry. The 5832 element wish will be used to simulate because it is accurate enough while being the least computationally expensive when compared with the 13824 and 27000 element meshes.

6.2. Flat Channel

As mentioned at the start of the chapter, the focus of the simulations is determining the temperature distribution on the upper wall (wall 1). This temperature distribution is compared with a solution using only conduction and convection. The comparison is characterised by the normalised temperature difference

$$\frac{T_{\text{rad}} - T_{\text{no rad}}}{\Delta T} = \frac{T_{\text{rad}} - T_{\text{no rad}}}{T_{\text{w2,B}} - T_{\text{in}}}. \tag{6.2}$$

The effects of the inlet temperature T_{in}, inlet velocity, and the difference between the wall temperature of wall 2 in Region B $T_{\text{w2,B}}$ and the inlet temperature T_{in} are also presented. The temperature contours shown have interpolated values between the nodes in the mesh.

6.2.1. Temperature Contours

The temperature contours of the upper wall (wall 1) are shown in Figures 6.6, 6.7, 6.8, and 6.9 for temperatures 525, 550, 575, and 600 °C, respectively. The shape of the temperature fields in these contours is similar for all temperatures. The sides of the channel (y=0 and y=0.15) have a higher temperature due to the effect of convection being lower at that region. The velocity near the edges is close to the minimum velocity specified by the Poiseuille velocity profile. The fluid flow brings less relatively cold fluid into this region, thus allowing the fluid to heat up more effectively. The temperature contours of the side and outlet at 575 °C can be seen in Figures 6.10 and 6.11.

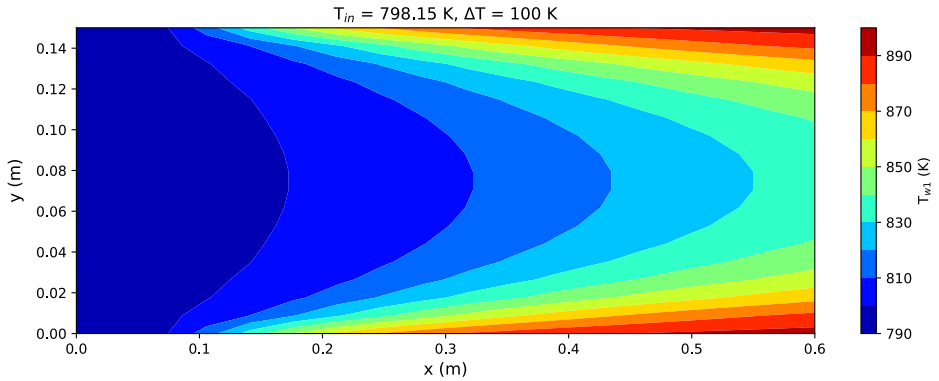

Figure 6.6: Temperature profile on wall 1 of the Flat Channel, with the input temperature $T_{\text{in}} = 525$ °C, the wall 2 temperature in Region B $T_{\text{w2,B}} = 625$ °C, and input velocity $v_{\text{in}} = 0.01111$ m/s which corresponds to a flow rate of 0.5 L/min.

The contours of just the temperature field don't clearly show the effect of thermal radiation transport. To understand the influence of thermal radiation, Figures 6.12, 6.13, and 6.14 show the difference between the temperature fields when incorporating and neglecting thermal radiation transport. The figures depict the normalised temperature of the top wall, the side wall, and the output of the Flat Channel geometry. Only the results with inlet temperature $T_{\text{in}} = 550$ °C are given since the results for the other temperatures look mostly the same. The differences between these profiles, caused by the inlet temperature and temperature differences between the upper and lower walls, will be further discussed in Sections 6.2.2 and 6.2.3.

Figures 6.12, 6.13, and 6.14 all show a temperature difference caused by thermal radiation transport in the upper wall, the sides, and the outlet of the Flat Channel. A part of the upper

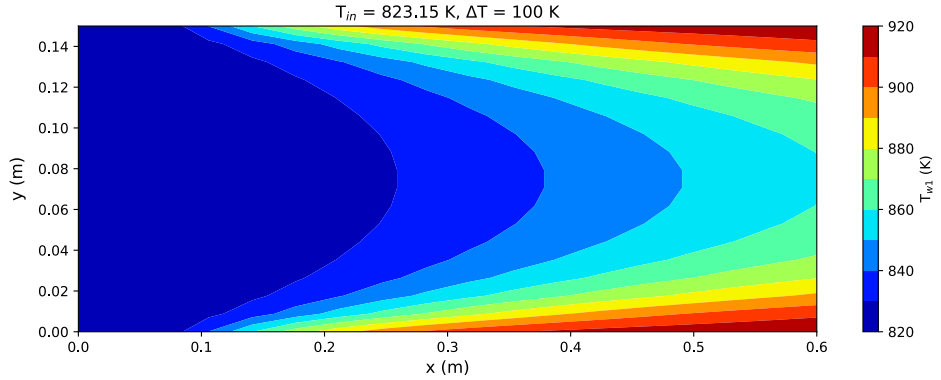

Figure 6.7: Temperature profile on wall 1 of the Flat Channel, with the input temperature $T_{\text{in}} = 550$ °C, the wall 2 temperature in Region B $T_{\text{w2,B}} = 650$ °C, and input velocity $v_{\text{in}} = 0.01111$ m/s which corresponds to a flow rate of 0.5 L/min.

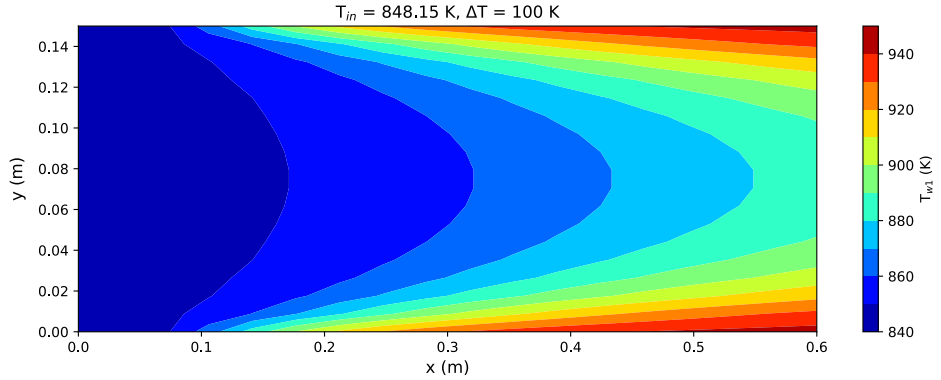

Figure 6.8: Temperature profile on wall 1 of the Flat Channel, with the input temperature $T_{\text{in}} = 575$ °C, the wall 2 temperature in Region B $T_{\text{w2,B}} = 675$ °C, and input velocity $v_{\text{in}} = 0.01111$ m/s which corresponds to a flow rate of 0.5 L/min.

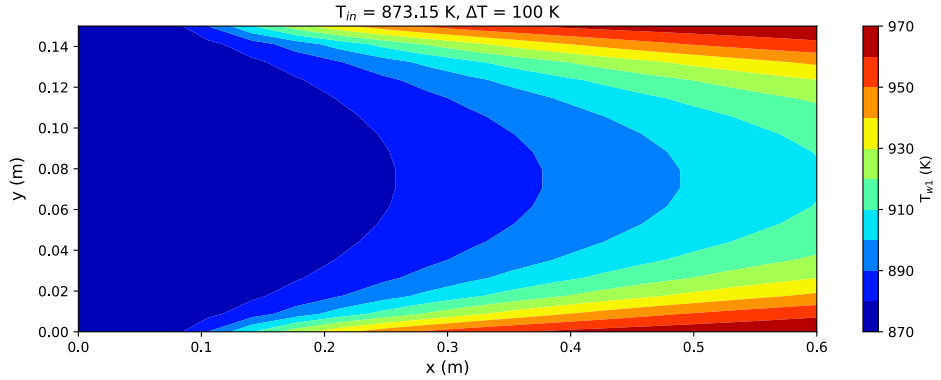

Figure 6.9: Temperature profile on wall 1 of the Flat Channel, with the input temperature $T_{\text{in}} = 600$ °C, the wall 2 temperature in Region B $T_{\text{w2,B}} = 700$ °C, and input velocity $v_{\text{in}} = 0.01111$ m/s which corresponds to a flow rate of 0.5 L/min.

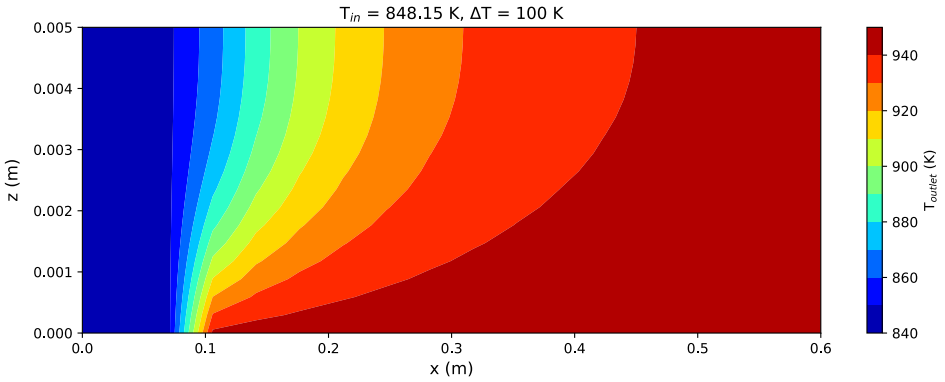

Figure 6.10: Temperature profile on wall 1 of the Flat Channel, with the input temperature $T_{\text{in}} = 600$ °C, the wall 2 temperature in Region B $T_{\text{w2,B}} = 700$ °C, and input velocity $v_{\text{in}} = 0.01111$ m/s which corresponds to a flow rate of 0.5 L/min.

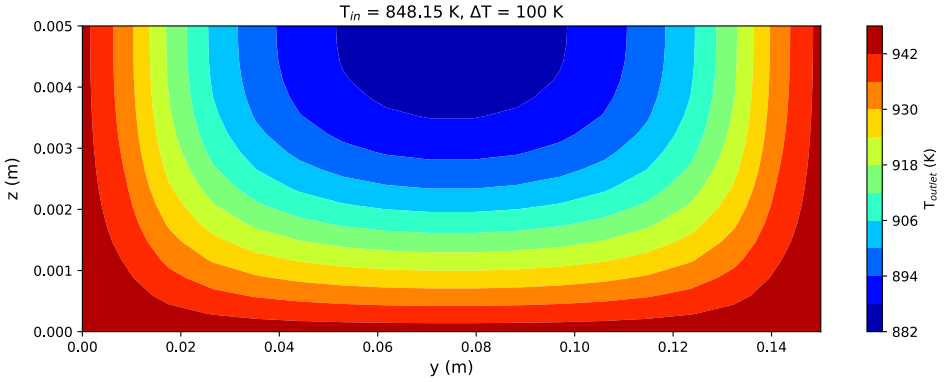

Figure 6.11: Temperature profile on wall 1 of the Flat Channel, with the input temperature $T_{\text{in}} = 600$ °C, the wall 2 temperature in Region B $T_{\text{w2,B}} = 700$ °C, and input velocity $v_{\text{in}} = 0.01111$ m/s which corresponds to a flow rate of 0.5 L/min.

wall heats up by approximately 1.5 °C more due to thermal radiation, while most other regions likewise heat up to a lesser extent. The only exceptions are Region A, where the temperature does not differ between the two models, and the zones near the sides of the Flat Channel, which are colder compared to the conduction-convection model. This cooling effect is partially due to thermal radiation sent from the hot regions near the side of the Flat Channel being more energetic, therefore having a lower attenuation coefficient, allowing it to travel further. The other part of the cooling effect is due to thermal radiation coming from the lower temperature areas next to the regions near the sides that have lower energy photons, causing the lost high energy by the hot parts to be insufficiently recovered, thus causing the cooling effect.

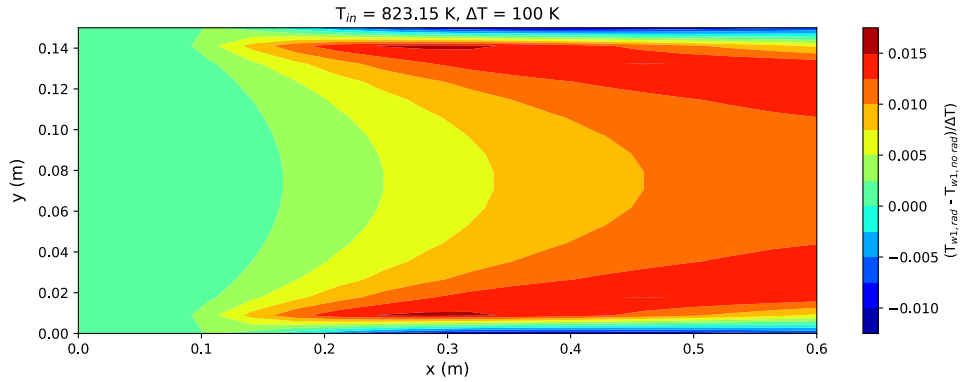

Figure 6.12: Normalised temperature difference profile on wall 1 of the Flat Channel, with the input temperature $T_{\text{in}} = 550$ °C, the wall 2 temperature in Region B $T_{\text{w2,B}} = 650$ °C, and input velocity $v_{\text{in}} = 0.01111$ m/s which corresponds to a flow rate of 0.5 L/min.

On the sides of the Flat Channel shown in Figure 6.13, the normalised temperature difference is higher at the start of Region B and lower near the top of Region B, excluding the beginning. The cooling effect is due to the same effect explained earlier. The heating effect is similar to the cooling effect but functions oppositely. The area at the start of Region B has a lower temperature compared to its surroundings in the positive x-direction, causing more energy to radiate into this region.

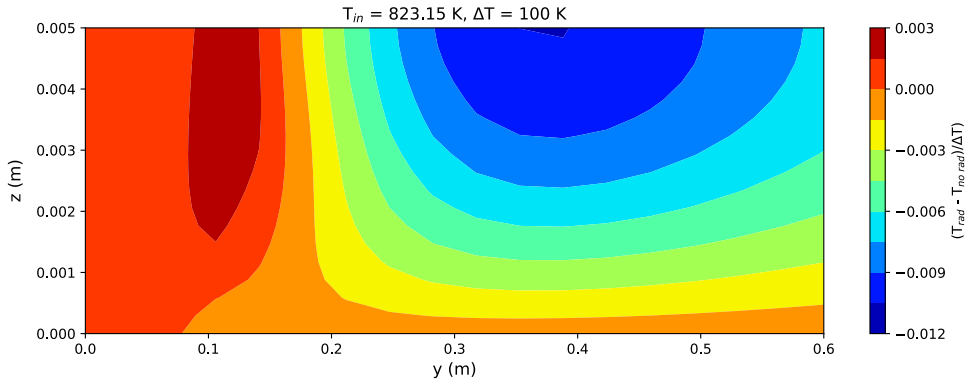

Figure 6.13: temperature difference profile on wall 1 of the Flat Channel, with the input temperature $T_{\text{in}} = 550$ °C, the wall 2 temperature in Region B $T_{\text{w2,B}} = 650$ °C, and input velocity $v_{\text{in}} = 0.01111$ m/s which corresponds to a flow rate of 0.5 L/min.

The normalised temperature difference contour of the outlet, seen in Figure 6.14, has two

symmetric sections of higher normalised temperature difference near the top wall of the Flat Channel and lower near the sides. This behaviour is due to the similar effect described for the upper wall of the Flat Channel. A gradient in the normalised temperature in the z-direction is also visible. This gradient is due to the effects of heat transport via thermal radiation and conduction becoming more apparent closer to the top wall.

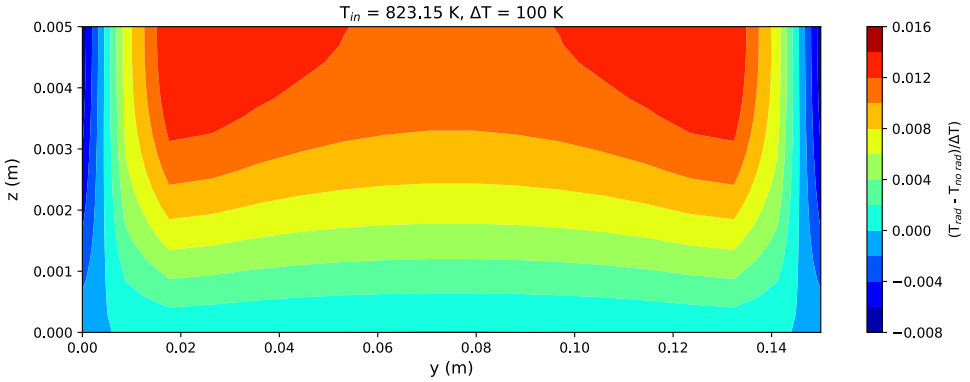

Figure 6.14: Normalised temperature difference profile on the outlet of the Flat Channel, with the input temperature $T_{\text{in}} = 550$ °C, the wall 2 temperature in Region B $T_{\text{w2,B}} = 650$ °C, and input velocity $v_{\text{in}} = 0.01111$ m/s which corresponds to a flow rate of 0.5 L/min.

6.2.2. Inlet Temperature

To determine the effect of inlet temperature T_{in} has on thermal radiation transport, the normalised temperature difference of the upper wall of the Flat Channel is compared using inlet temperature $T_{\text{in}} = 525, 550, 575, 600, 700,$ and 1000 °C. Only the normalised temperature difference contours of the upper wall with inlet temperatures of 525 and 1000 °C are shown because the other temperature contours have similar shapes. The temperature contours can be seen in Figures 6.15 and 6.16. They have similar shapes compared to the normalised temperature difference contours shown in Section 6.2.1.

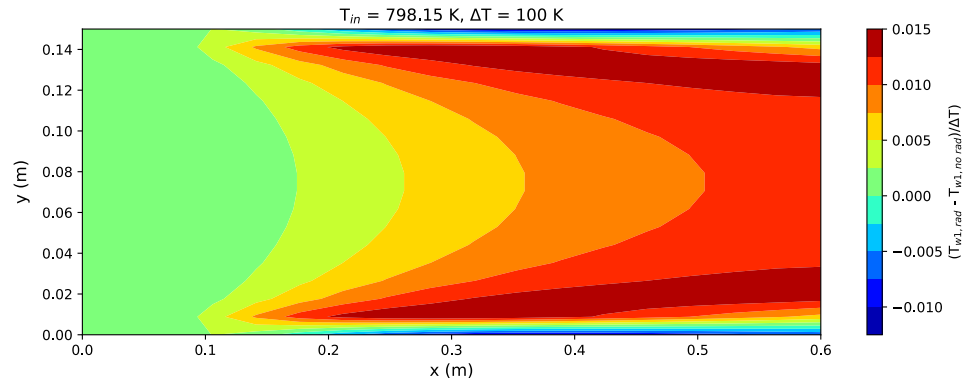

Figure 6.15: Normalised temperature difference contour on wall 1 of the Flat Channel. The inlet temperature $T_{\text{in}} = 1000$ °C, input velocity $v_{\text{in}} = 0.01111$ m/s and the wall 2 temperature in Region B $T_{\text{w2,B}} = 1100$ °C.

The normalised temperature difference values on the nodes of elements along the centre line of the upper wall (wall 1) are compared for the different inlet temperatures. This comparison is seen in Figure 6.17, where the normalised temperature difference is on the vertical axis, and the x-coordinate of the centre line is on the horizontal axis.

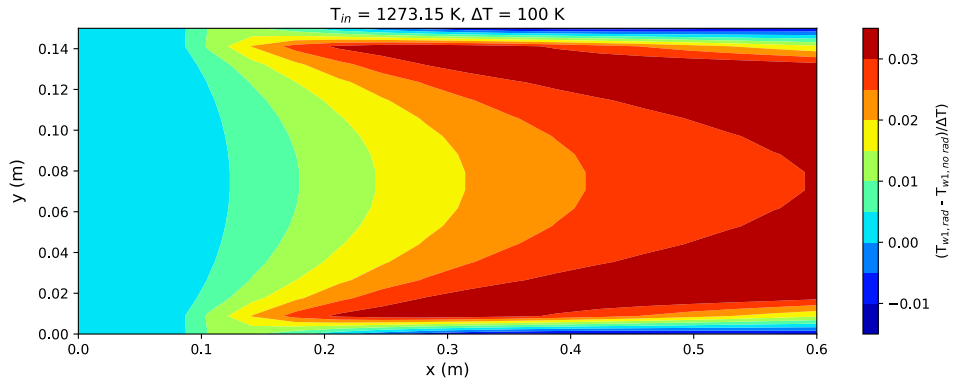

Figure 6.16: Normalised temperature difference contour on wall 1 of the Flat Channel. The inlet temperature $T_{\text{in}} = 1000$ °C, input velocity $v_{\text{in}} = 0.01111$ m/s and the wall 2 temperature in Region B $T_{\text{w2,B}} = 1100$ °C.

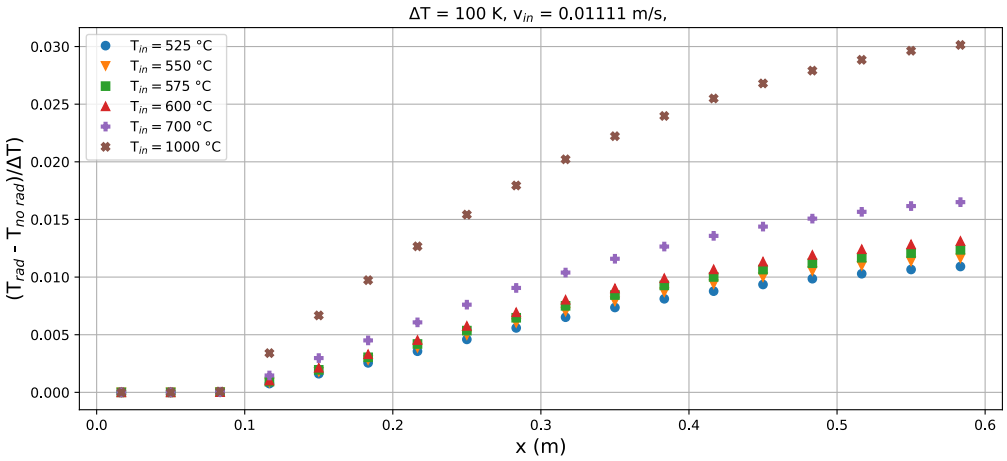

Figure 6.17: Normalised temperature difference profiles on wall 1 of the Flat Channel along the centre line. The inlet velocity $v_{\text{in}} = 0.01111$ m/s and the wall 2 temperature in Region B $T_{\text{w2,B}} = T_{\text{in}} + 100$ °C.

Figure 6.17 shows that an increase in inlet temperature increases the normalised temperature difference on the upper wall, indicating a better transport of thermal radiation. This increase is expected since transport via thermal radiation scales with T^4, so higher inlet temperatures will cause more thermal radiation to be emitted in every location.

6.2.3. Wall Temperature

The temperature difference between the lower wall (wall 2) in Region B and the inlet temperature also affects thermal radiation transport. The normalised temperature differences when having a temperature difference $dT = 5, 25, 50,$ and 100 °C can be seen in Figures 6.18, 6.19, 6.20, and 6.21. These figures look similar to each other but with small differences. To more accurately compare these normalised temperature differences, the centre line of the upper wall will again be plotted, which results in Figure 6.22.

Similar to the effect seen from the inlet temperature, the temperature difference between the lower wall (wall 2) in Region B and the inlet temperature also increases thermal radiation transport. The reason for this increase is comparable to the inlet temperature dependence.

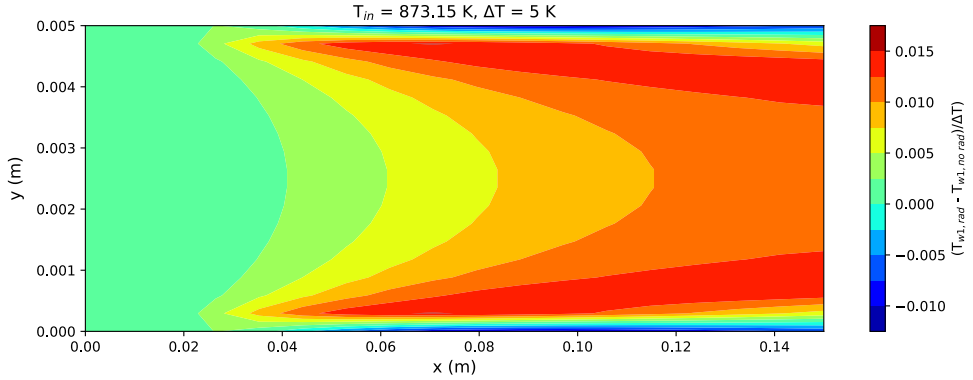

Figure 6.18: Normalised temperature difference contour on wall 1 of the Flat Channel. The wall 2 temperature in Region B $T_{\text{w2,B}} = 605$ °C, the inlet temperature $T_{\text{in}} = 600$ °C, and the inlet velocity $v_{\text{in}} = 0.01111$ m/s.

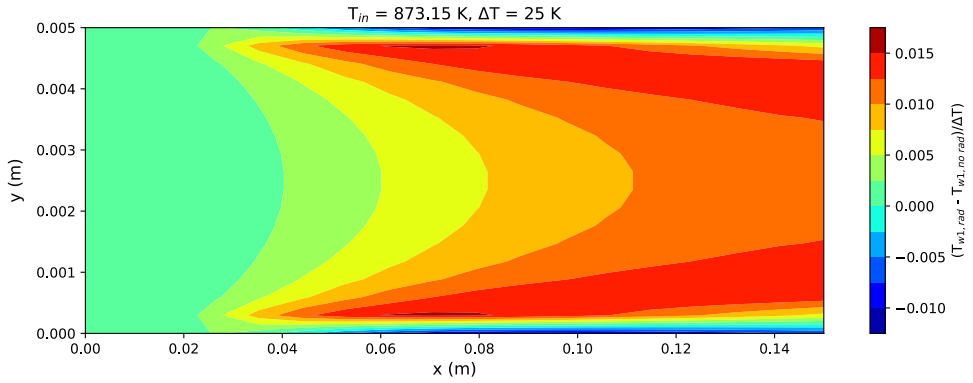

Figure 6.19: Normalised temperature difference contour on wall 1 of the Flat Channel. The wall 2 temperature in Region B $T_{\text{w2,B}} = 625$ °C, the inlet temperature $T_{\text{in}} = 600$ °C, and the inlet velocity $v_{\text{in}} = 0.01111$ m/s.

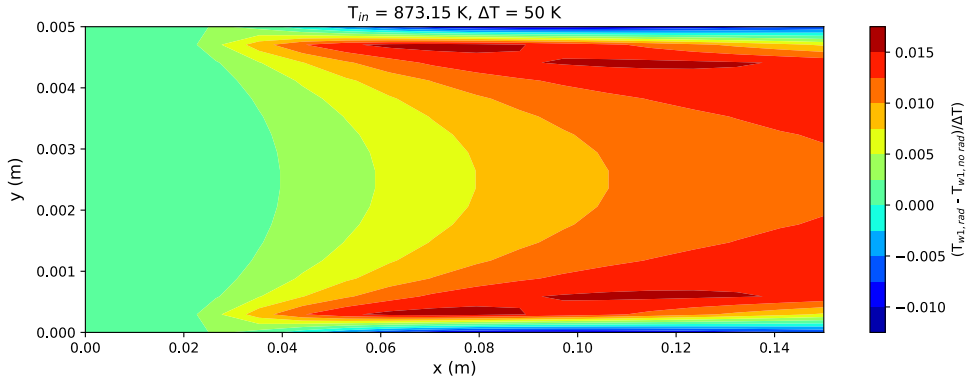

Figure 6.20: Normalised temperature difference contour on wall 1 of the Flat Channel. The wall 2 temperature in Region B $T_{\text{w2,B}} = 650$ °C, the inlet temperature $T_{\text{in}} = 600$ °C, and the inlet velocity $v_{\text{in}} = 0.01111$ m/s.

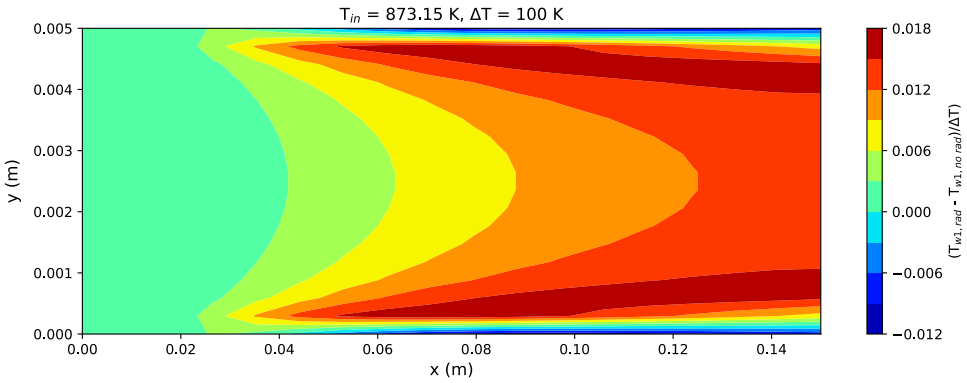

Figure 6.21: Normalised temperature difference contour on wall 1 of the Flat Channel. The wall 2 temperature in Region B $T_{w2,B} = 700$ °C, the inlet temperature $T_{in} = 600$ °C, and the inlet velocity $v_{in} = 0.01111$ m/s.

The area near the bottom has a high temperature, causing the fluid near the bottom wall to radiate higher energy photons that can travel better to the upper wall since they have a lower attenuation coefficient.

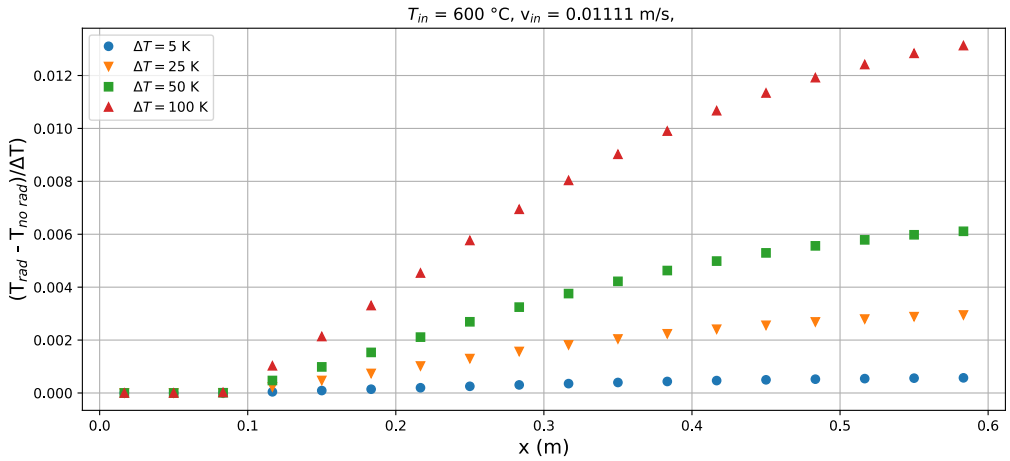

Figure 6.22: Normalised temperature difference profiles on wall 1 of the Flat Channel along the centre line. The inlet temperature $T_{in} = 600$ °C and the wall 2 temperature in Region B $T_{w2,B}$ is 5, 25, 50, or 100 °C higher than the inlet temperature.

6.2.4. Input Velocity

The last of three parameters that is varied is the input velocity. The temperature contour and the normalised temperature difference contour with different inlet velocities $v_{\text{in}} = 0.001, 0.005, 0.01111, 0.02222,$ and 0.04444 m/s are presented. Figures 6.23, 6.24, 6.25, 6.26, and 6.27 show the temperature contours of the different input velocities with constant input temperature $T_{\text{in}} = 525$ °C and the lower wall temperature in Region B $T_{\text{w2,B}} = 625$ °C.

Unlike the changes caused by the variation of inlet temperatures and wall temperatures, a change in inlet velocity is more impactful on the shape of the temperature contour of the upper wall. Lower inlet velocities negate the dominating influence of convection and allow conduction and thermal radiation to have a more observable effect on the heat transport in the Flat Channel. The high-temperature areas near the side of the Flat Channel grow in width the lower the input velocity. In Figure 6.23, where the input velocity $v_{\text{in}} = 0.001$ m/s, the high-temperature areas have grown so large they have combined. On the opposite side of the spectrum, Figure 6.27 shows tiny high-temperature zones due to the large velocity $v_{\text{in}} = 0.04444$ m/s.

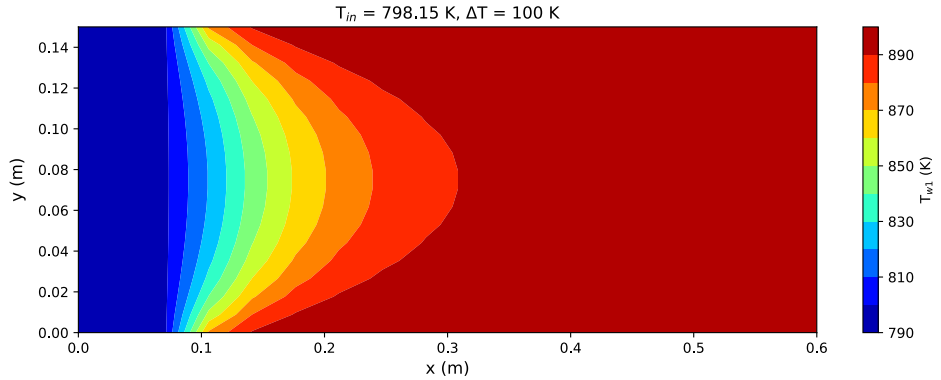

Figure 6.23: Temperature profile on wall 1 of the Flat Channel, with input velocity $v_{\text{in}} = 0.001$ m/s. The input temperature $T_{\text{in}} = 525$ °C and the wall 2 temperature in Region B $T_{\text{w2,B}} = 625$ °C.

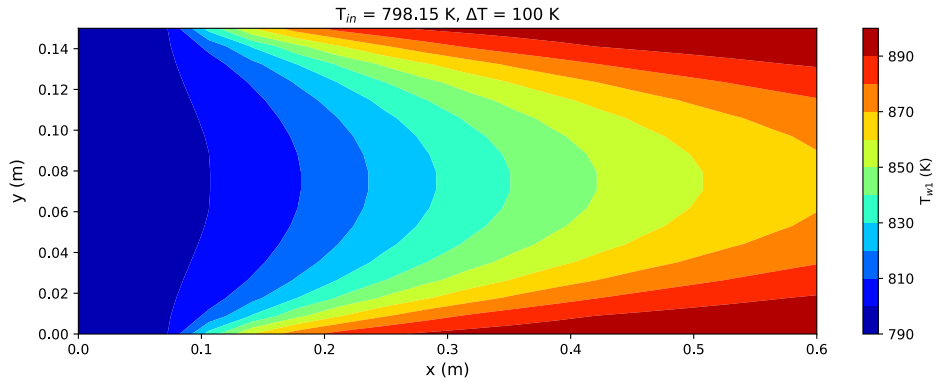

Figure 6.24: Temperature profile on wall 1 of the Flat Channel, with input velocity $v_{\text{in}} = 0.005$ m/s. The input temperature $T_{\text{in}} = 525$ °C and the wall 2 temperature in Region B $T_{\text{w2,B}} = 625$ °C.

Dissimilar to the normalised temperature difference contours when varying the inlet temperature and wall temperature, the inlet velocity shows clear distinctions in the shape. From Figures 6.28, 6.29, 6.30, 6.31, and 6.32, it looks like the shape of the normalised temperature difference contour ”stretches” out more in the x-direction the higher the inlet velocity. The nor-

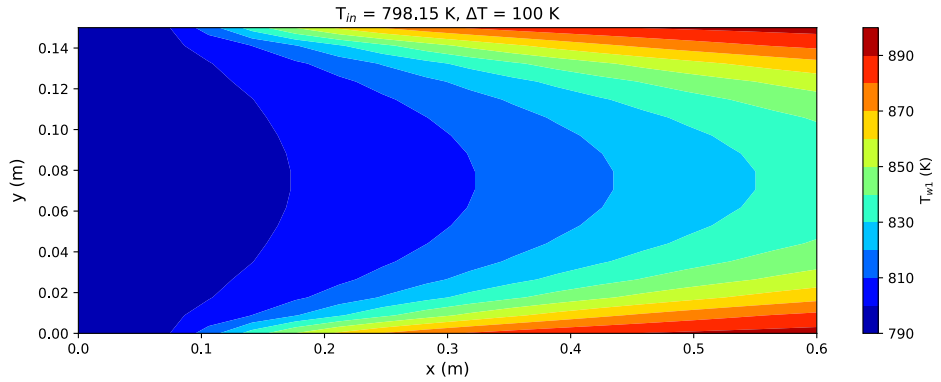

Figure 6.25: Temperature profile on wall 1 of the Flat Channel, with input velocity $v_{\text{in}} = 0.01111$ m/s. The input temperature $T_{\text{in}} = 525$ °C and the wall 2 temperature in Region B $T_{\text{w2,B}} = 625$ °C.

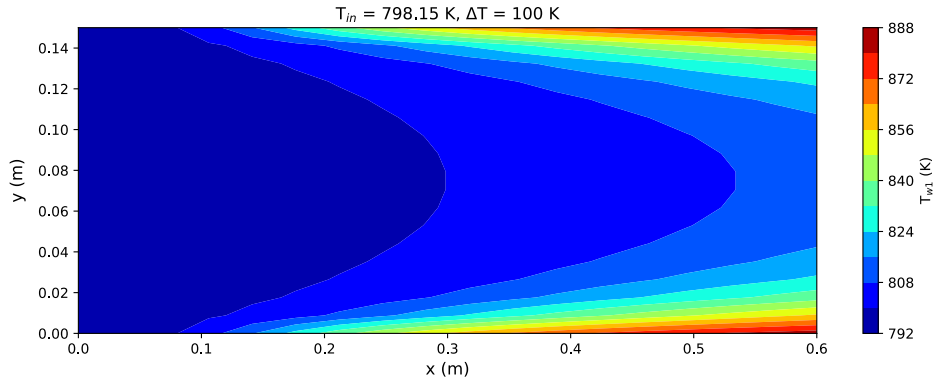

Figure 6.26: Temperature profile on wall 1 of the Flat Channel, with input velocity $v_{\text{in}} = 0.02222$ m/s. The input temperature $T_{\text{in}} = 525$ °C and the wall 2 temperature in Region B $T_{\text{w2,B}} = 625$ °C.

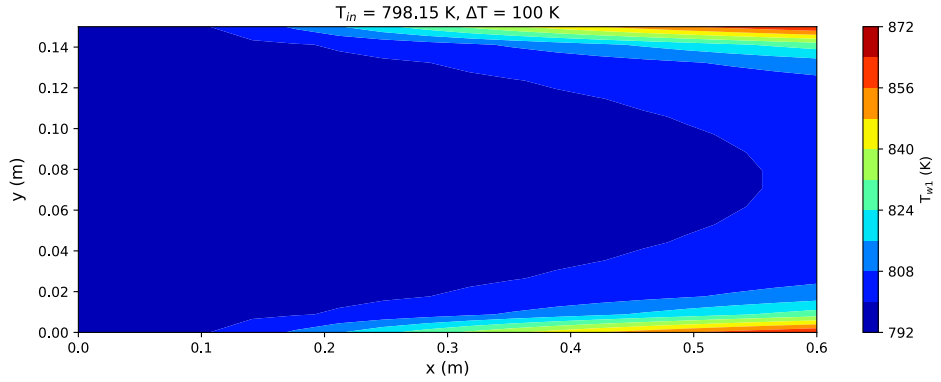

Figure 6.27: Temperature profile on wall 1 of the Flat Channel, with input velocity $v_{\text{in}} = 0.04444$ m/s. The input temperature $T_{\text{in}} = 525$ °C and the wall 2 temperature in Region B $T_{\text{w2,B}} = 625$ °C.

malised temperature difference seen in Figure 6.28 is near the boundary of Regions A and B, where the lower wall temperature has a jump in temperature. The higher temperature region on the positive x side causes more thermal radiation to enter the lower temperature region near the jump. The lower temperature area loses less energy due to its lower emission spectrum, causing the area to heat up. Higher inlet velocities ”stretch” this effect into the normalised temperature differences seen in Figures 6.29, 6.30, 6.31, and 6.32.

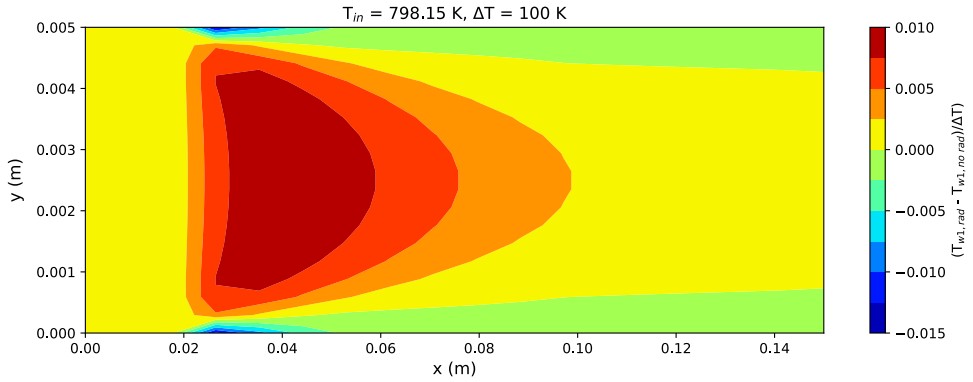

Figure 6.28: Normalised temperature difference profile on wall 1 of the Flat Channel along the centre line. The input velocity $v_{\text{in}} = 0.001$ m/s, the input temperature $T_{\text{in}} = 525$ °C, and the wall 2 temperature in Region B $T_{\text{w2,B}} = 625$ °C.

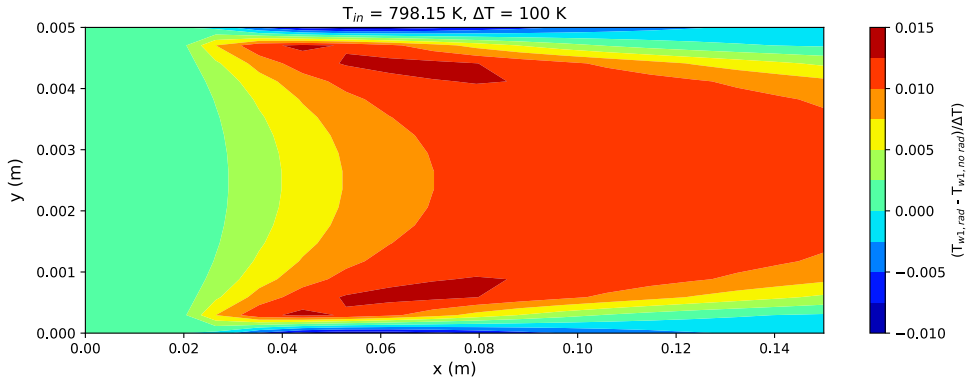

Figure 6.29: Normalised temperature difference profile on wall 1 of the Flat Channel along the centre line. The input velocity $v_{\text{in}} = 0.005$ m/s, the input temperature $T_{\text{in}} = 525$ °C, and the wall 2 temperature in Region B $T_{\text{w2,B}} = 625$ °C.

The differences caused in the normalised temperature difference by the inlet velocity along the centre line of the upper wall can be seen in Figure 6.33. The effect of thermal radiation increases with a lowering of the inlet velocity up to a certain point. At the lowest input velocity, the normalised temperature difference becomes more localised and decreases compared to the inlet velocity of 0.005 m/s. A reason for this might be that conduction becomes the predominant transport mechanism. Another point to note from this graph is that there appears to be a certain input velocity that causes a maximum effect of thermal radiation transport compared to the other heat transport mechanisms. This specific input velocity appears to be between 0.001 and 0.01111 m/s.

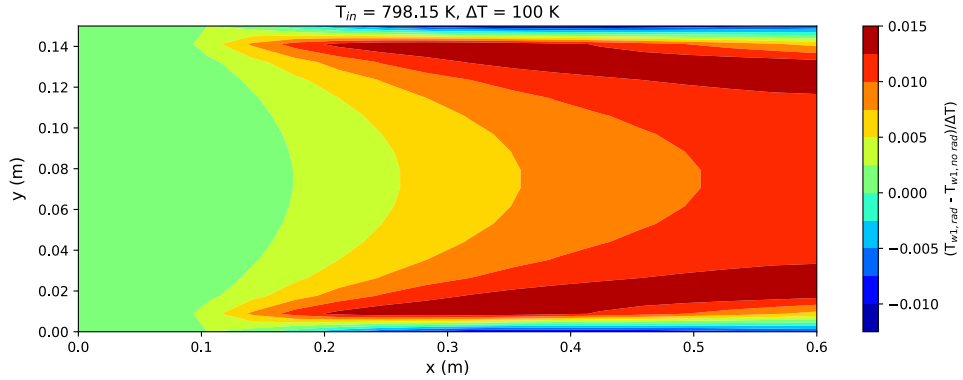

Figure 6.30: Normalised temperature difference profile on wall 1 of the Flat Channel along the centre line. The input velocity $v_{\text{in}} = 0.01111$ m/s, the input temperature $T_{\text{in}} = 525$ °C, and the wall 2 temperature in Region B $T_{\text{w2,B}} = 625$ °C.

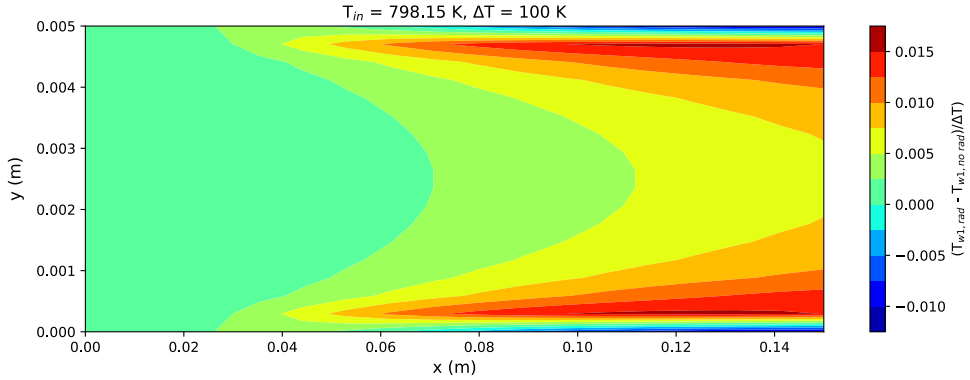

Figure 6.31: Normalised temperature difference profile on wall 1 of the Flat Channel along the centre line. The input velocity $v_{\text{in}} = 0.02222$ m/s, the input temperature $T_{\text{in}} = 525$ °C, and the wall 2 temperature in Region B $T_{\text{w2,B}} = 625$ °C.

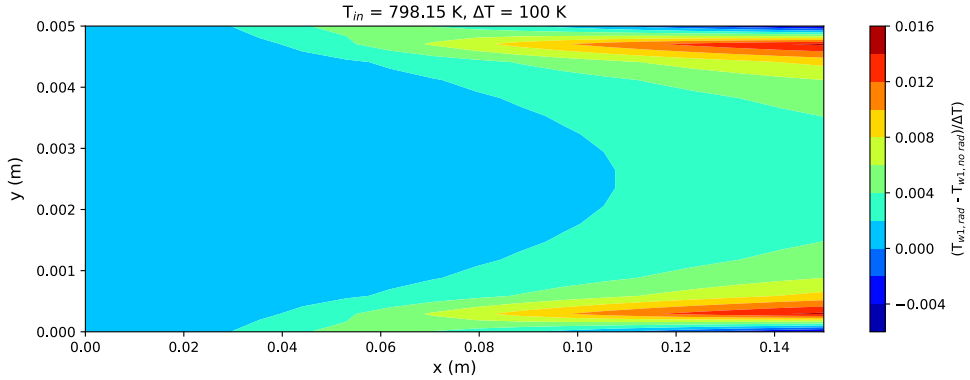

Figure 6.32: Normalised temperature difference profile on wall 1 of the Flat Channel along the centre line. The input velocity $v_{\text{in}} = 0.04444$ m/s, the input temperature $T_{\text{in}} = 525$ °C, and the wall 2 temperature in Region B $T_{\text{w2,B}} = 625$ °C.

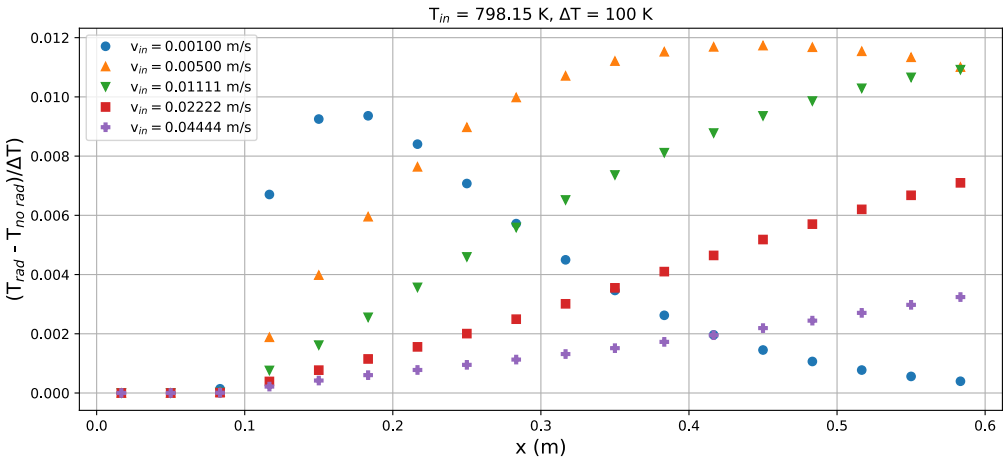

Figure 6.33: Normalised temperature difference profiles on wall 1 of the Flat Channel along the centre line. The input velocities are $v_{\text{in}} = 0.001, 0.005, 0.01111, 0.0222,$ and 0.04444 m/s, the input temperature $T_{\text{in}} = 525$ °C, and the wall 2 temperature in Region B $T_{\text{w2,B}} = 625$ °C.

6.3. Discussion

The results show a rise in temperature on the upper wall when incorporating thermal radiation. This temperature rise is small compared to the temperature distribution from the simulation using only convection and conduction. For the input parameters used in the SWATH experiment, the temperature increase was below three degrees Celsius when using a wall temperature 100 °C higher than the inlet. For instance, an inlet velocity of inlet temperature of 550 °C and a lower wall temperature in Region B of 650 °C give a maximum difference of 1.5 °C at the top wall. The temperature is higher than 600 °C in the area with the maximum normalised temperature difference. From these temperatures, it can be concluded that thermal radiation only accounts for at most less than 1.5/(600-550) = 3% of the total increase in temperature. This is similar to the result obtained from the master thesis of Merten (2022, [31]), which concluded that the normed divergence of conduction contributes about 65 times more to the total temperature field than the normed divergence of radiative intensity.

Another point of note is the diffuse reflectivity. The reflectivities used came from the data of a stainless steel mirror, which has a low diffuse reflectivity and a large specular reflectivity. The real-life situation might be different, which means this simulation is an incorrect example of reality. Apart from the reflectivity values, the FLiNaK parameters were taken as constant and independent of temperature. This temperature independence is not valid in real life. The density, thermal conductivity, specific heat capacity, viscosity, and absorption coefficients are all temperature-dependent.

Also, it was assumed the molten salt had no contaminants, which is not always true. The unpure salt can deposit impurities on the walls, thus increasing their diffuse reflectivity.

The radiation model assumed the inlet and outlet of the Flat Channel had the same boundary condition. The inlet and outlet do not have this boundary condition in real life, as there is no boundary to reflect off of. This boundary condition should not be a problem as the real-life scenario has molten salt with similar temperatures to the inlet and outlet temperatures that radiate thermal radiation into the geometry.

Generally, one mesh should be used to solve the radiation part of the code and a different mesh to solve the energy balance or total heat transport. This simulation did not use two meshes but one mesh for both models. Using one mesh causes an error near the edges of the mesh. The temperature contours are Δx in the x-direction, Δy in the y-direction, or Δz in the z-direction away from the actual edge. Δz = 0.278 mm, so this should be close enough to give a good idea of the genuine wall temperature. $\Delta x = 33.333$ mm and $\Delta y = 8.333$ mm.

7

Conclusion

Nuclear power is a reliable power source that does not depend on fossil fuels, contributing much less greenhouse gasses into the atmosphere. The negatives of nuclear energy are nuclear waste and substantial safety concerns. To mitigate these detrimental effects, alternative reactor designs like the Molten Salt Reactor (MSR), which uses molten salt instead of water, are researched. One research target is the transport of thermal radiation inside molten salt. Thermal radiation becomes more apparent at higher temperatures, like in MSRs, and molten salt is not opaque to thermal radiation like water. The SWATH facility researches the effect of thermal radiation using the salt FLiNaK. To simulate the Flat Channel geometry used in SWATH, a simulation model was created. The lower wall of the Flat Channel geometry is hotter than the inflowing FLiNaK to see if thermal radiation can have a noticeable effect on the upper wall.

Thermal radiation, caused by black-body radiation, behaves according to the Radiation Transport Equation (RTE). Thermal radiation can be absorbed or scattered by a medium but does not require a medium to transfer heat, like conduction and convection. The scattering of thermal radiation inside a pure medium is negligible. To solve the RTE, the interaction of thermal radiation with a boundary must be known. Thermal radiation can be absorbed, diffusely reflected, or specularly reflected by an opaque boundary.

The simulation model consists of two parts: one that solves the RTE using the Discrete Ordinates Method (DOM) and another that solves the energy balance (which incorporates conduction, convection, and thermal radiation) using the Finite Volume Method (FVM) with the Gauss-Seidel method to obtain the temperature field of the Flat Channel.

The simulation resulted in a temperature increase of less than 3% due to thermal radiation transport. Higher FLiNaK temperatures flowing into the Flat Channel and higher bottom wall temperatures increase the effect of thermal radiation transport. The lower the inlet velocity, the higher the effect of thermal radiation transport is up to a certain point, after which the influence of thermal radiation decreases.

References

[1] Office of Nuclear Energy, *Advantages and challenges of nuclear energy*, Mar. 2021. [Online]. Available: https://www.energy.gov/ne/articles/advantages-and-challenges-nuclear-energy.

[2] IEA, *The Role of Critical World Energy Outlook Special Report Minerals in Clean Energy Transitions*. May 2021. [Online]. Available: https://iea.blob.core.windows.net/assets/ffd2a83b-8c30-4e9d-980a-52b6d9a86fdc/TheRoleofCriticalMineralsinCleanEnergyTransitions.pdf.

[3] European Commission, Directorate-General for Internal Market, Industry, Entrepreneurship and SMEs, S. Bobba, *et al.*, *Critical raw materials for strategic technologies and sectors in the EU : a foresight study*. Publications Office, 2020. DOI: 10.2873/58081.

[4] Energy Education, *Molten salt reactor*, 2015. [Online]. Available: https://energyeducation.ca/encyclopedia/Molten_salt_reactor.

[5] World Nuclear Association, *Molten salt reactors*, May 2021. [Online]. Available: https://world-nuclear.org/information-library/current-and-future-generation/molten-salt-reactors.aspx.

[6] International Atomic Energy Agency, *Molten salt reactors*, Apr. 2016. [Online]. Available: https://www.iaea.org/topics/molten-salt-reactors.

[7] W. Yang, T. Parker, H. Ladouceur, and R. J. Kee, "The interaction of thermal radiation and water mist in fire suppression," *Fire Safety Journal*, vol. 39, no. 1, pp. 41–66, 2004, ISSN: 0379-7112. DOI: 10.1016/j.firesaf.2003.07.001.

[8] OpenStax, *Appendix e – water properties*. [Online]. Available: https://psu.pb.unizin.org/eshanichemistry110/back-matter/appendix-e-water-properties/.

[9] SAMOSAFER, Dec. 2022. [Online]. Available: https://samosafer.eu/.

[10] N. Capellan, V. Ghetta, J. Giraud, and P. Rubiolo, "Simulation models and safety assessment for fluid-fuel energy reactors — SAMOSAFER, D5.3 Report on SWATH experiments," Tech. Rep., 2023.

[11] J. Howell, M. Menguc, and R. Siegel, *Thermal Radiation Heat Transfer, 6th Edition*. Taylor & Francis, 2015, ISBN: 9781466593268.

[12] M. F. Modest, *Radiative Heat Transfer*, Third Edition. Academic Press, 2013, ISBN: 978-0-12-386944-9.

[13] M. Rubel, G. De Temmerman, J. Coad, *et al.*, "Mirror test for international thermonuclear experimental reactor at the jet tokamak: An overview of the program," *Review of Scientific Instruments*, vol. 77, p. 5, Jun. 2006. DOI: 10.1063/1.2202915.

[14] C. N. A. C. Z. Bahri, W. M. Al-Areqi, M. '. F. M. Ruf, and A. A. Majid, "Characteristic of molten fluoride salt system LiF-BeF2 (Flibe) and LiF-NaF-KF (Flinak) as coolant and fuel carrier in molten salt reactor (MSR)," *AIP Conference Proceedings*, vol. 1799, no. 1, p. 040 008, Jan. 2017, ISSN: 0094-243X. DOI: 10.1063/1.4972932. eprint: https://pubs.aip.org/aip/acp/article-pdf/doi/10.1063/1.4972932/13734989/040008_1_online.pdf.

[15] S.-C. Lee, Y. Zhai, Z. Li, *et al.*, "Comparative studies of the structural and transport properties of molten salt flinak using the machine-learned neural network and reparametrized classical forcefields," *The Journal of Physical Chemistry B*, vol. 125, no. 37, pp. 10 562–10 570, 2021, PMID: 34496565. DOI: 10.1021/acs.jpcb.1c05608.

[16] J. Lane, H. MacPherson, F. Maslan, and A. Weinberg, "Fluid fuel reactors: Molten salt reactors, aqueous homogeneous reactors, fluoride reactors, chloride reactors, liquid metal reactors and why liquid fission," in (Addison-Wesley books in nuclear science and metallurgy), Addison-Wesley books in nuclear science and metallurgy. Addison-Wesley Publishing Company, 1958, ch. 12. [Online]. Available: https://moltensalt.org/references/static/downloads/pdf/FFR_chap12.pdf.

[17] L. Ponomarev, M. Seregin, and A. Parshin, "Choice of the fuel salt for the molten salt reactor," *At. Energ.*, vol. 115, pp. 6–11, Jan. 2013. [Online]. Available: https://www.researchgate.net/publication/284119683_Choice_of_the_fuel_salt_for_the_molten_salt_reactor.

[18] E. S. Chaleff, "The radiative heat transfer properties of molten salts and their relevance to the design of advanced reactors," Ph.D. dissertation, Ohio State University, 2016. [Online]. Available: http://rave.ohiolink.edu/etdc/view?acc_num=osu1480539289737113.

[19] M. Tano Retamales, "Developement of multi-physical multiscale models for molten salts at high temperature and their experimental validation," Theses, Université Grenoble Alpes, Nov. 2018. [Online]. Available: https://theses.hal.science/tel-02007262.

[20] *Quantum ESPRESSO*, Mar. 2022. [Online]. Available: https://www.quantum-espresso.org/.

[21] P. R. Tulip, "Dielectric and lattice dynamical properties of molecular crystals via density functional perturbation theory: Implementation within a first principles code," Ph.D. dissertation, Durham University, 2004. [Online]. Available: https://core.ac.uk/download/pdf/6116467.pdf.

[22] E. E. Lewis and W. F. Miller, *Computational methods of Neutron Transport*. Wiley, 1984.

[23] K. D. Lathrop and B. G. Carlson, "Discrete ordinates angular quadrature of the neutron transport equation," Los Alamos Scientific Lab., N. Mex., Tech. Rep., 1964. [Online]. Available: https://digital.library.unt.edu/ark:/67531/metadc1033703/m2/1/high_res_d/4666281.pdf.

[24] V. Khokhlov, I. Korzun, V. Dokutovich, and E. Filatov, "Heat capacity and thermal conductivity of molten ternary lithium, sodium, potassium, and zirconium fluorides mixtures," *Journal of Nuclear Materials*, vol. 410, no. 1, pp. 32–38, 2011, ISSN: 0022-3115. DOI: 10.1016/j.jnucmat.2010.12.306.

[25] D. Williams, "Assessment of candidate molten salt coolants for the NGNP/NHI heat-transfer loop," Jan. 2006. [Online]. Available: https://moltensalt.org/references/static/downloads/pdf/ORNL-TM-2006-29.pdf.

[26] A. Rudenko, A. Redkin, E. Il'ina, *et al.*, "Thermal conductivity of flinak in a molten state," *Materials*, vol. 15, no. 16, 2022, ISSN: 1996-1944. DOI: 10.3390/ma15165603.

[27] J. Ambrosek, M. Anderson, K. Sridharan, and T. Allen, "Current status of knowledge of the fluoride salt (flinak) heat transfer," *Nuclear Technology*, vol. 165, no. 2, pp. 166–173, 2009. DOI: 10.13182/NT165-166.

[28] J. Cibulková, M. Chrenková, R. Vasiljev, V. Kremenetsky, and M. Boča, “Density and viscosity of the (lif + naf + kf)eut (1) + k2taf7 (2) + ta2o5 (3) melts,” *Journal of Chemical & Engineering Data*, vol. 51, no. 3, pp. 984–987, 2006. DOI: 10.1021/je050490g.

[29] S. Patankar, *Numerical Heat Transfer and Fluid Flow* (Series in computational methods in mechanics and thermal sciences). Taylor & Francis, 1980, ISBN: 9780891165224.

[30] G. Wu, Y.-T. Lin, P. Dong, and K. Zhang, “Development of two-dimensional non-hydrostatic wave model based on central-upwind scheme,” *Journal of Marine Science and Engineering*, vol. 8, p. 505, Jul. 2020. DOI: 10.3390/jmse8070505.

[31] B. Merten, “Radiative heat transfer in molten salt reactors,” M.S. thesis, Delft University of Technology, 2022.

A

Appendix

Extra Figures

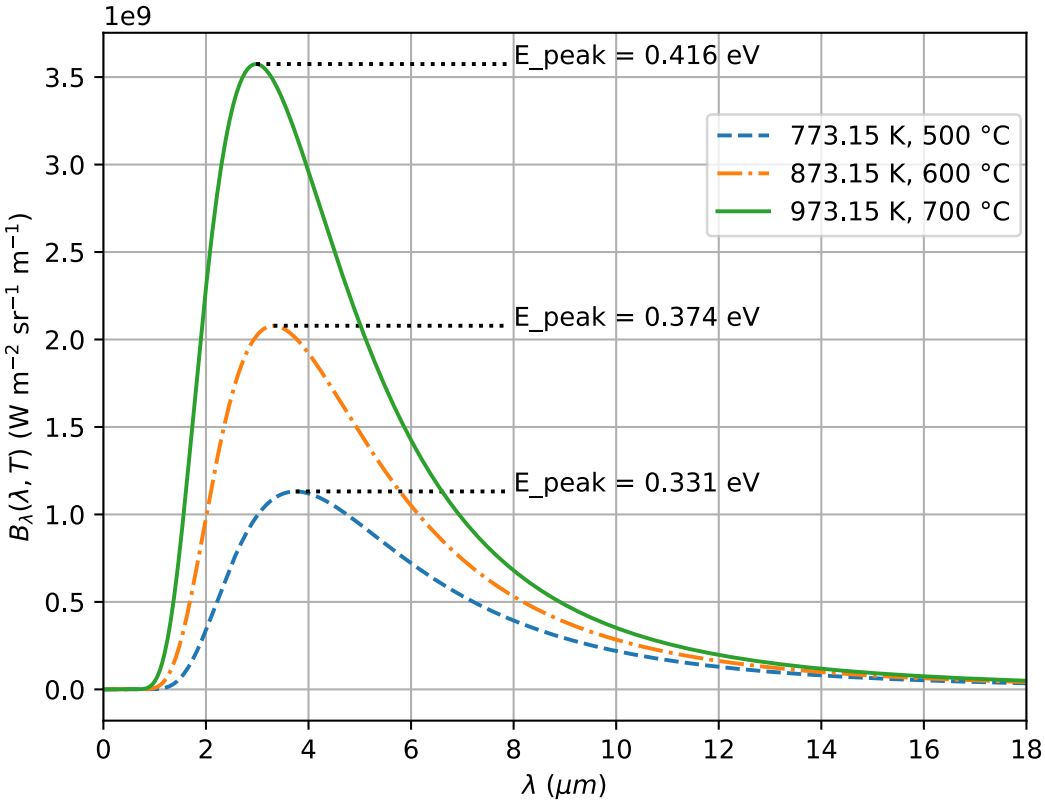

Figure A.1: Planck's law for black bodies is shown using temperatures of 500, 600, and 650 degrees Celsius. The photon wavelength λ is on the horizontal axis, and the corresponding spectral radiative intensity $B_\lambda(\lambda, T)$ is on the vertical axis. The mode energy at the maximum spectral irradiance is also visible.

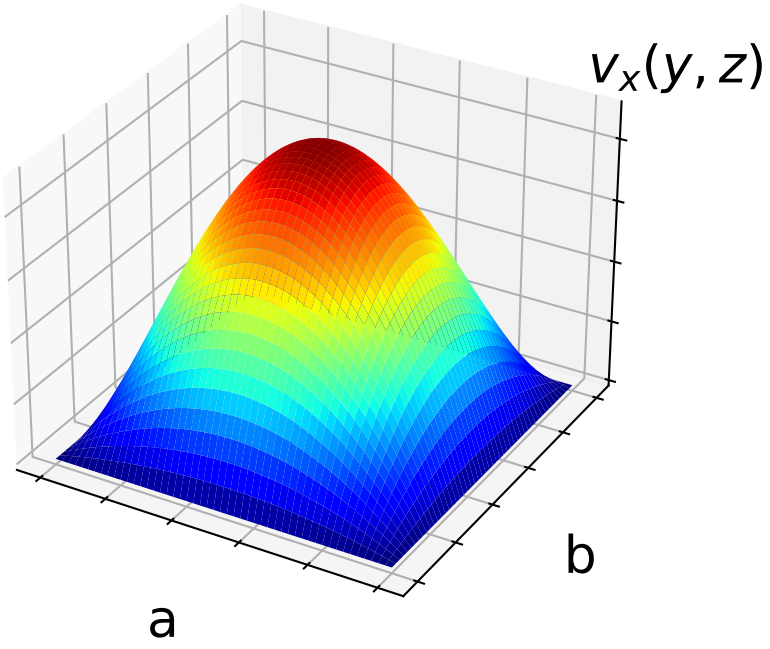

Figure A.2: The three-dimensional Poiseuille velocity profile used in the simulations.

Parameters Info

The different FLiNaK parameters found in literature which were averaged to get the parameters used in the simulations. $c_p = 0.66 + 1.37 \cdot 10^{-3}T \pm 0.013 = 1.893 \pm 0.013$; $\lambda = 0.36 + 5.6 \cdot 10^{-4}T \pm 0.01 = 0.864 \pm 0.01$ 900K [24]

$\rho = 2579.3 - 0.6240T \pm 0.25 = 2017.7 \pm 0.25$ kg m^{-3}; $\mu = e^{-3.0489+3847/T} \pm 0.0052 = 3.40602 \pm 0.0052$ mPa·s 900 K [28]

$\rho = 2621.2333 + 0.651333T = 2035.0$ kg m^{-3} 900 K (Average of three methods) [15]

$\rho = 2579.3–0.6240T = 2017.7$; $\mu = 0.0248e^{4477/T} = 3.58778$ mPa·s; $c_p = 1.88$; $\lambda = 0.36 + 5.6 \cdot 10^{–4}T = 0.864$ 900 K [25] (2020)